Mon. Not. R. Astron. Soc. **000**, 1–?? (2003) Printed 22 July 2003 (MN LATEX style file v2.2)

Discriminating between unresolved point sources and "negative" SZ clusters in CMB maps

J.A. Rubiño-Martín[1,2]⋆ and R.A. Sunyaev[1,3]
[1] *Max-Planck Institut für Astrophysik, Karl-Schwarzschild-Str. 1, D-85740 Garching, Germany*
[2] *Instituto de Astrofisica de Canarias, C/ Via Lactea, s/n, 38200 La Laguna, Tenerife, Spain*
[3] *Space Research Institute (IKI), Russian Academy of Sciences, Moscow, Russia*

ABSTRACT

Clusters of galaxies produce negative features at wavelengths $\lambda > 1.25$ mm in CMB maps, by means of the thermal SZ effect, while point radio sources produce positive peaks. This fact implies that a distribution of unresolved SZ clusters could be detected using the negative asymmetry introduced in the odd-moments of the brightness map (skewness and higher), or in the probability distribution function (PDF) for the fluctuations, once the map has been filtered in order to remove the contribution from primordial CMB fluctuations from large scales. This property provides a consistency check to the recent detections from CBI and BIMA experiments of an excess of power at small angular scales, in order to confirm that they are produced by a distribution of unresolved SZ clusters. However it will require at least 1.5 - 2 times more observing time than detection of corresponding power signal. This approach could also be used with the data of the planned SZ experiments (e.g. ACT, AMI, AMIBA, APEX, 8 m South Pole telescope).

Key words: cosmology: cosmic microwave background – cosmology: observations – galaxies: clusters: general.

1 INTRODUCTION

Fluctuations in the Cosmic Microwave Background (CMB) radiation can provide information about hot gas in galaxy clusters over a wide range of redshifts (Sunyaev & Zeldovich 1972,1980 (hereafter SZ), and Birkinshaw 1999; Carlstrom, Holder, & Reese 2002). On arcminute angular scales and smaller, the thermal SZ contribution to the CMB anisotropy is expected to dominate that of the primary anisotropies (Sunyaev & Zeldovich 1970, Springel, White, & Hernquist 2001 (hereafter SWH), Holder 2002). A new generation of experiments is measuring the CMB sky at these angular scales. In particular, two recent experiments, BIMA (Dawson et al. 2002) and CBI (Mason et al. 2002), both observing at frequencies around 30 GHz, have detected an excess of power in the multipole region $\ell \gtrsim 2000$, where the SZ power is expected to be dominant over the CMB signal. Nevertheless, at these observing frequencies, radio point sources are known to also produce a significant contribution to the power (Longair & Sunyaev 1969; Franceschini et al. 1989; Toffolatti et al. 1998) if they are not subtracted properly from the CMB maps. The reported detections of power have argued that this point-source contamination is not a problem, thus suggesting that the signal could be due to the SZ effect (Dawson et al. 2002; Bond et al. 2002; Komatsu & Seljak 2002). These arguments are based on analytical models or simulations of what we would expect to measure. Thus, it would be interesting to explore, in a model-independent way, the nature of these contributions. The importance of this topic has been stressed recently by Cooray & Melchiorri (2002), who suggested to use a cross-correlation of CMB maps with maps of the large scale structure. This idea has been applied for this purpose to other datasets with larger angular resolutions (e.g. Banday et al. 1996, to the COBE data, or Rubiño-Martín, Atrio-Barandela, & Hernández-Monteagudo 2000, to the Tenerife data).

Here, we propose a general model-independent method to determine if the measured power excess in a *single-frequency* map is (mainly) due to point sources or SZ clusters. To this end, we use the fact that for frequencies below 217 GHz ($\lambda > 1.25$ mm), the thermal SZ effect produces negative features in the maps, while the point sources produce positive peaks. We illustrate this fact with figure 1, where we show two simulated one-dimensional maps, one of SZ clusters observed at $\nu = 30$ GHz, and the other one of point sources. Dotted lines show the original (without sources of any kind) zero level of fluctuations, while dashed lines show the observed (average) zero level once the mean of the map has been subtracted. With the same level of fluctuations (same rms at the observed scale), a power spectrum

⋆ E-mail:jalberto@mpa-garching.mpg.de, jalberto@ll.iac.es

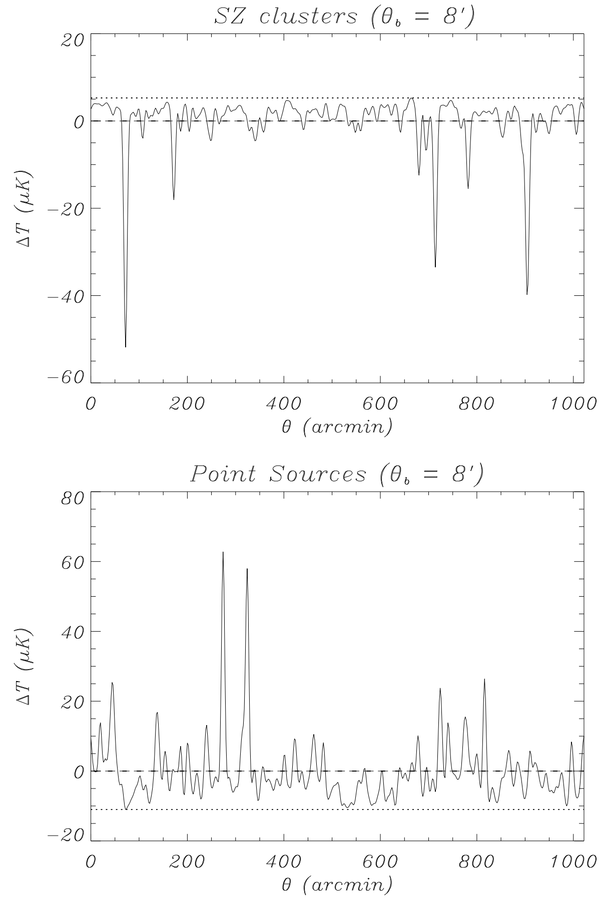

Figure 1. One dimensional map of a single realisation of SZ clusters (upper panel) and point sources (lower panel), observed with a gaussian beam of $8'$ full-width half-maximum, and no noise. Dashed lines show the average (zero) level of fluctuations, while dotted lines show the original zero level before subtracting the mean to the map. With the same level of fluctuations, the C_ℓ analysis does not permit to distinguish between these two cases. Therefore, we need to use the skewness, or to proceed with an analysis of the asymmetry of the $P(D)$ curve in order to separate these two cases.

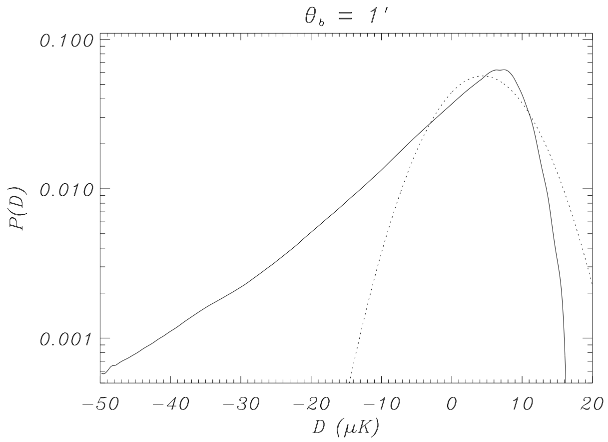

Figure 2. Example of the strong non-gaussianity of the P(D) function for SZ clusters. We present the P(D) function for a SZ map in the Rayleigh-Jeans region of the spectrum, where clusters are "negative" sources. For comparison, it is also shown the best gaussian fit to this P(D) curve ($\sigma = 6.1\ \mu K$). This curve will be explained in detail in section 7.

analysis is not able to distinguish these two cases, so we need to use an statistic carrying information about the sign of the subjacent signal (e.g. the skewness) to suggest the nature of the objects producing this excess of power. The existence of negative skewness at $\lambda > 1.25$ mm, while positive skewness at $\lambda < 1.25$ mm, is a clear prediction for SZ clusters.

We investigate here the discrimination between positive and negative sources using the probability distribution function (PDF) for the observed flux. From a given map, *the PDF function can be obtained easily as an histogram of the (normalised) number of pixels within a given flux interval.* This tool has been widely used in radio astronomy when studying the statistical properties of a background of point sources (Scheuer 1957; Cavaliere et al. 1973; Condon 1974), because in that case the shape of this function is strongly related with the statistical properties of the sources (i.e. theirs spatial distribution). In this context, this function is known as the 'deflection probability distribution', or the $P(D)$ curve. This '$P(D)$ formalism' has been successfully applied to study the diffuse X-ray background (Scheuer 1974; Fabian 1975; Cavaliere & Setti 1976; Condon & Dressel 1978), as well as to determine the contribution of discrete point sources to CMB maps (Franceschini et al. 1989; Toffolatti et al. 1998). For the CMB, if we assume the standard inflationary scenario, then the primordial fluctuations are gaussian, so the $P(D)$ itself is a gaussian, as well as for the standard instrumental noise. However, the main characteristic of this $P(D)$ curve for point sources (Franceschini et al. 1989) or for SZ clusters (Cole & Kaiser 1988) is its non-gaussianity. Typical curves for a $P(D)$ distribution of point sources or SZ clusters will exhibit long tails (see Figure 2). The point is that at $\lambda > 1.25$ mm, sources will produce a positive tail, while SZ clusters will give a negative one. It is important to mention that at $\lambda < 1.25$ mm, both AGNs and SZ-clusters will produce positive tails. Then it is necessary to use other characteristics of both populations (frequency spectra, etc) to distinguish them. As an illustration, Figure 3 demonstrates P(D) for SZ sources at four frequencies, ν = 107 and 150 GHz (where clusters are giving negative signal) and 270 and 520 GHz (where the signal from clusters is positive, and exactly opposite in sign to the previous cases).

2 SZ CLUSTERS AS NEGATIVE SOURCES

It is possible to consider clusters of galaxies as "extended sources" with a peculiar spectrum given by (Sunyaev 1980)

$$F_{\nu_z}(\theta) = B_{\nu_z}(T_r)\frac{\delta I_\nu(\theta)}{I_\nu} = \frac{2(kT_r)^3}{(hc)^2}\frac{kT_e}{m_e c^2}g(x)\tau_T(\theta) \qquad (1)$$

where τ_T is the optical depth for Thompson scattering, $x = h\nu/kT_{cmb}$ is the dimensionless frequency, with $\nu_z = \nu(1+z)$ and $T_r = T_{cmb}(1+z)$, so that x does not depend on redshift z, and

$$g(x) = \frac{x^3}{e^x-1}f(x) = \frac{x^4 e^x}{(e^x-1)^2}[x coth(x/2) - 4] \qquad (2)$$

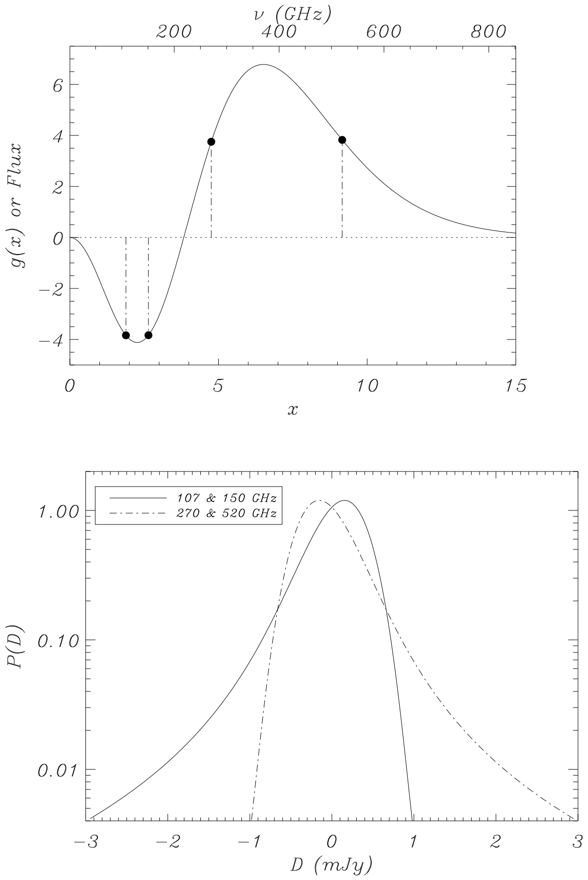

Figure 3. P(D) function for SZ clusters at different frequencies. First panel shows the $g(x)$ function (see equation (2)), and four frequencies ($\nu = 107$, 150, 270 and 520 GHz) where this function (and so the flux density) takes the same absolute value. Second panel shows the P(D) function for these four cases, using a simple truncated power-law to model the cluster source counts (see section 4), with values $n(S) = 28$ $(\mathrm{S/1Jy})^{-2.5}$ sr^{-1} Jy^{-1} at 150 GHz, truncating at $S_0 = 0.1$ mJy, and with angular resolution $\theta_b = 1'$. The P(D) function is presented relative to its average value, so the distribution for the cases $\nu = 107$ GHz and 150 GHz is symmetric around zero respect to the other two cases.

is the spectral shape factor. Note that this shape factor includes the term from B_ν, the Planck function, and $\delta I_\nu / I_\nu$ and $f(x)$ are the formulae for the CMB spectrum distortions due to Comptonization from Zeldovich & Sunyaev (1969). From here, two different but equivalent approaches can be used to estimate the spectral luminosity of the cluster. We can obtain the spectral luminosity by just integrating the change of the CMB intensity due to scattering by individual electrons of temperature $T_e(r)$ over the cluster volume (Sunyaev 1980)

$$L_{\nu_z}(x,z) = 8\pi \frac{(kT_{cmb})^3}{(hc)^2} \sigma_T g(x) (1+z)^3 4\pi \int \frac{kT_e(r)}{m_e c^2} n_e(r) r^2 dr \quad (3)$$

This expression, for the case of isothermal intergalactic gas, is proportional to the total amount of electrons in the cluster, because in that case $\frac{4\pi}{3} \int n_e(r) r^2 dr = M_{IGG}/(\mu_e m_p)$, where M_{IGG} is the mass of the hot intergalactic gas, and μ_e is the mean molecular weight per electron. The important point here is that clusters increase rapidly their spectral luminosities with redshift ($L_{\nu_z} \propto (1+z)^3$). Taking into account the luminosity distance to the source $d_L(z)$, we can obtain the spectral flux as $S_\nu = \frac{L_\nu(z)}{4\pi d_L^2(z)}$.

On the other hand, according to Korolev, Sunyaev, & Yakubsev (1986), we can use the central value of the Comptonization parameter for the cluster

$$y_C = \int \frac{kT_e(l)}{m_e c^2} \sigma_T n_e(l) dl \quad (4)$$

For a given y_C, the surface brightness of the cluster does not depend on redshift. Then, the flux from the cluster is equal to

$$S_\nu(x) = 2\pi\theta_0^2 \frac{(kT_r)^3}{(hc)^2} g(x) y_C Y(\theta/\theta_0) \quad (5)$$

where θ_0 corresponds to the angular dimension of the cluster core radius, and the $Y(\theta/\theta_0)$ function takes into account the angular dependence of y over the cluster image. One important conclusion from this point of view of the problem is that clusters with given physical parameters should have a minimum flux at some redshift, due to the well-known redshift dependence of the angular dimension of the cluster with a given core radius. In the Universe with $\Omega = 1$ we have minimum angular dimension at $z = 1.25$ [1], and at higher z, both angular distance and the flux will increase: clusters with given physical parameters have minimum flux where its angular dimension is minimum. It is important to note that

(i) for an experiment with an angular resolution θ_b larger than the core radius of clusters ($\theta_b \gg \theta_0$), they will be unresolved objects, and therefore they will appear as point sources for us;

(ii) according to the dependence of $g(x)$ from x, these point sources will have "positive" flux at $\lambda < 1.25$ mm, and "negative" flux at $\lambda > 1.25$ mm.

(iii) for given physical parameters, clusters show a minimum flux at that redshift z where the angular dimension is minimal. On the other hand, the observed source counts depend on the luminosity function. For instance, if we use the Press-Schechter formalism (Press & Schechter 1974, hereafter PS), then we have a divergence of the (comoving) number density of objects at low masses (i.e. low fluxes). Nevertheless, we know that cooling and feedback play an important role in the SZ predictions, so we do not expect to find bright SZ clusters with masses below few times $10^{13} M_\odot$. Then, it is necessary to introduce a low mass cutoff in PS formalism in order to derive realistic SZ predictions, as it has been done by several authors (e.g. de Luca, Desert, & Puget 1995; Komatsu & Kitayama 1999; Molnar & Birkinshaw 2000). Thus, we expect to observe a minimum flux and a minimum angular dimension for SZ clusters.

Several authors have studied the contribution of the SZ effect to the power spectrum of CMB fluctuations at small scales, both theoretically (e.g. Cooray 2001) or using simulations (e.g. SWH, Zhang, Pen & Wang 2002). In any case,

[1] For a cosmological model with $\Omega_m = 0.3$ and $\Omega_\Lambda = 0.7$, this happens at $z = 1.60$.

the main observational emphasis is put on the power spectrum (C_ℓ), because it is easier to measure than, for example, the bispectrum. When determining if the excess of power at low scales detected by CBI and BIMA is due to SZ clusters, the comparison has been done in terms of the power spectrum (Dawson et al. 2002; Bond et al. 2002; Komatsu & Seljak 2002). However, when we are working with the power spectrum, we are losing information about the sign of the fluctuations, so we need to find the skewness, or to proceed with an analysis of the asymmetry of the $P(D)$ function.

3 STATISTICAL DESCRIPTION OF RANDOMLY DISTRIBUTED POSITIVE/NEGATIVE SOURCES

The formalism relating the (differential) source counts and the PDF (or $P(D)$ function) of the observed deflection D at a given point, due to a population of poissonian-distributed unresolved sources, was first discussed by Scheuer (1957), and extended by Condon (1974). This analytical approach will permit us to understand much more deeply the observed shapes of the $P(D)$ curves, and to relate them with the underlying source counts.

Using the standard notation from radio astronomy, let $n(S)$ be the differential counts per solid angle, at a given frequency ν, and let $b(\theta,\phi)$ the response of a radio telescope to a point source (normalised to 1 at the peak). Let $s = Sb(\theta,\phi)$ be the response of the instrument to a source of flux density S located at a given distance (θ,ϕ) of the beam centre. Then, the mean number of source responses of flux between s and $s+ds$ in the beam, $R(s)$, is given by

$$R(s) = \int n\left[\frac{s}{b(\theta,\phi)}\right]\frac{d\Omega}{b(\theta,\phi)} \tag{6}$$

The relationship between $n(S)$ (or $R(s)$) and the $P(D)$ function, for the case of a pencil beam antenna, is given in terms of the characteristic functions of $R(s)$ and $P(D)$, which can be written as $r(w)$ and $p(w)$, respectively. The equations are

$$r(w) = \int_{-\infty}^{+\infty} R(s)\exp(2\pi i w s)ds \tag{7}$$

$$p(w) = \exp[r(w) - r(0)] \tag{8}$$

and the $P(D)$ function can be obtained as the inverse Fourier transform

$$P(D) = \int_{-\infty}^{+\infty} p(w)\exp(-2\pi i w D)dw = \int_{-\infty}^{+\infty}\exp(r(w) - r(0) - 2\pi i w D)dw \tag{9}$$

This relation can be also employed in the case of tracking interferometers (Fomalont et al. 1988, 1993), using the CLEANed map. For the case of a phase switch interferometer, the above relations still holds, but replacing Fourier transforms by Bessel transforms (Scheuer 1957).

It should be noted that these expressions are general, and therefore valid for the case of negative sources. Indeed, from the previous equations it follows that *if a population of positive sources $n(S)$, with $S > 0$, is described by the function $P(D)$, then the population of sources $n(|S|)$, with $S < 0$, is described by $P(-D)$*. Thus, in this section, we will restrict ourselves to study distributions of positive sources ($n(S) = 0$ for $S < 0$), given that we can obtain the corresponding distribution for negative sources with the transformation $P(D) \rightarrow P(-D)$.

All the equations described through this section are implicitly assuming non-resolved objects. Rowan-Robinson & Fabian (1974) have studied the modifications introduced by extended sources, showing that the condition for unresolved objects applies until $\theta_b \approx \theta_s$, where θ_s is the typical size of the source, and θ_b the beam size.

3.1 Analytical cases

Let us consider here several particularly simple but useful cases for the $n(S)$ function, which can be treated analytically. These cases will be used later. For a more general case of source counts, we can use a Monte Carlo method to work out the P(D) distribution (e.g. Hewish (1961)). First of all, we will consider a power-law shape, $n(S) = KS^{-\beta}$, with $S > 0$. As a second case, we will also consider a truncated power-law at a certain flux density S_0, i.e. $n(S) = 0$ for $S < S_0$, and $n(S) = KS^{-\beta}$, for $S > S_0$. Hereafter, we will assume that S is given in Jy, so we are implicitly writing $n(S) = K(S/1Jy)^{-\beta}$, and the units for K are $\mathrm{Jy}^{-1}\,\mathrm{sr}^{-1}$. We will also assume a gaussian antenna pattern, described as $b(\theta) = \exp(-\frac{1}{2}(\theta/\sigma_b)^2)$, where σ_b is the width of the beam, and $\theta_b = \sqrt{8\log 2}\sigma_b$ its full-width half maximum (FWHM).

In these cases, the $R(s)$-function can be analytically obtained. Following Condon (1974), we define the effective solid angle (Ω_e) as

$$\Omega_e = \int [b(\theta,\phi)]^{\beta-1}d\Omega = \frac{\pi\theta_b^2}{4(\beta-1)\log 2} \tag{10}$$

We then obtain $R(s) = K\Omega_e s^{-\beta}$ for a pure power-law, and

$$R(s) = \begin{cases} K\Omega_e s^{-\beta}, & s > S_0 \\ K\Omega_e S_0^{-\beta}\frac{S_0}{s}, & s < S_0 \end{cases} \tag{11}$$

for a power-law truncated below S_0 and the gaussian beam. From these equations, it is straight-forward to obtain numerically the $P(D)$ function. These problems have been studied by Scheuer (1957) and Condon (1974) for the power law case[2], and by Scheuer (1974) (analytically) and Hewish (1961) (numerically) for the truncated case.

Finally, it is also interesting to consider the case of a power-law source counts with an upper cut-off in flux, S_c. This is the expression to use in order to compute the $P(D)$ function from a map where the brightest sources have been subtracted down to the flux S_c. Therefore, if $n(S) = KS^{-\beta}$ for $S_0 < S < S_c$, and 0 elsewhere, then

$$R(s) = \begin{cases} K\Omega_e s^{-1}(S_0^{1-\beta} - S_c^{1-\beta}), & s < S_0 \\ K\Omega_e s^{-\beta}(1 - (\frac{s}{S_c})^{\beta-1}), & S_0 < s < S_c \\ 0, & s > S_c \end{cases} \tag{12}$$

[2] For the power law case, Condon (1974) gives an analytic expression for $p(w)$, which is valid for $2 < \beta < 3$, so in these cases the numerical calculation is even easier.

3.2 Confusion noise

Apart from the $P(D)$ function, it is also interesting to characterise the properties of the source population by the moments of the $R(s)$ distribution. For a pure power-law expression for the number-flux-density relation, it is clear that the nth-moment of the R-distribution is

$$< s^n >= \int_0^{s_c} s^n R(s) ds = \frac{K\Omega_e s_c^{n+1-\beta}}{n+1-\beta}, \qquad n = 1, 2, 3, ... (13)$$

where s_c represents the cutoff value for point-source subtraction. For the truncated power-law case, the nth-moment of this distribution is

$$< s^n >= \frac{K\Omega_e s_c^{n+1-\beta}}{n+1-\beta} - \frac{\beta-1}{n(n+1-\beta)} K\Omega_e S_0^{n+1-\beta} \qquad (14)$$

The second moment of the $R(s)$ function ($\sigma_c^2 =< s^2 >$) has been extensively used to characterise the 'confusion noise', i.e. the noise due to the presence of faint unresolved sources inside the beam (Scheuer 1957). Normally, the adopted criterion for the detection of sources is such as the intensity q times the sigma of the map, so the minimum subtraction threshold can be written as $s_c = q\sigma_c$, being $q = 3-5$ the usual values. Thus, inserting this condition in equation (13), we obtain for the power-law case:

$$\sigma_c(q) \equiv \left[\frac{q^{3-\beta}}{3-\beta} K\Omega_e \right]^{1/(\beta-1)} \qquad (15)$$

where we explicitly write that σ_c depends on q for this choice of the subtraction threshold. Note that this threshold can be decreased if we use measurements at higher angular resolution. We will discuss this in section 8.

For the power-law source counts, it is easy to show that the flux at which we have one source every X beam areas, S_X, can be written as

$$S_X(Jy) = \left(K\Omega_e X \right)^{1/(\beta-1)} \qquad (16)$$

From these last two equations, we immediately see that for the flux level $s_c = q\sigma_c(q)$, we have one source every $q^2/(3-\beta)$ beam areas. For the particular case of $\beta = 2.1$ and $q = 5$, this expression takes the value ~ 28, so we recover the well-known result that if we have more than one source of a given flux every 30–40 beam areas (it depends on β), we will be limited by confusion noise. We should remind here that the $P(D)$ function provides information (roughly) down to the flux S_1 at which we have one source per beam area (Scheuer 1974).

3.3 Scaling of P(D) with frequency

To conclude this section, we will derive the scaling of $P(D)$ with frequency for SZ clusters. This scaling can be derived from the one for the source counts, which is given by

$$n(S;\nu) = \left| \frac{g(x_0)}{g(x)} \right| n\left(S\frac{g(x_0)}{g(x)}; \nu_0 \right) \qquad (17)$$

where $x_0 = h\nu_0/kT_{cmb}$. This equation is similar to the one obtained by Condon (1984) for the scaling of the differential source counts of point sources with power-law spectra ($S \propto \nu^{-\alpha}$) [3]. From here, we obtain

$$P(D;\nu) = \left| \frac{g(x_0)}{g(x)} \right| P\left(D\frac{g(x_0)}{g(x)}; \nu_0 \right) \qquad (18)$$

We see that clusters of galaxies should be described by a single $P(D)$ function, which is the same at all frequencies (but rescaled) if θ_b is the same, and which is equivalent to the PDF for the y parameter. However, our description permits the use of the main characteristic of the effect, the existence of negative sources. Therefore, if we compare data from two frequencies, one above $\nu = 217$ GHz and the other one below, then in the first case the $P(D)$ for clusters will exhibit a positive tail while in the second case, a negative tail, being in both cases described by the same (rescaled) $P(D)$ function. If we now use this expression to derive the moments of the $P(D)$ function, we obtain

$$< D^n; \nu >= \left[\frac{g(x)}{g(x_0)} \right]^n < D^n; \nu_0 >, \qquad n = 1, 2, 3, ... \quad (19)$$

Therefore, we explictly see that the normalised moments of a map of thermal SZ clusters (with no noise), $< D^n > /\sigma^n$, are exactly the same in magnitude for all frequencies, but we have a change of sign in all the (normalised) odd-moments when we cross the frequency $\nu = 217$ GHz.

4 SOURCE COUNTS FOR RADIO SOURCES AND CLUSTERS

As we have seen in the last section, the shape of the $P(D)$ function for (positive/negative) sources provides a means of determining the underlying source counts. Therefore, we will discuss here which are the typical source counts both for radio sources and SZ clusters.

4.1 Radio point sources

Several authors (e.g. Fischer & Lange 1993) have studied the contribution to the confusion limits from different populations of extragalactic sources. In the context of CMB measurements at frequencies close to $\nu \sim 30$ GHz, radio sources are known to produce the main contribution to the confusion noise. Because of this reason, recent experiments have used a source subtraction technique, and thus have produced source counts for these radio sources. These curves are well fitted by power-laws in the flux density region around a few mJy. Typical values for the K and β parameters, at frequencies around 30 GHz, are $n(S) \approx 54\ (S_{34\ GHz}/1Jy)^{-2.15}$ sr^{-1} Jy^{-1}, for $S_{34\ GHz} > 60$ mJy (from the VSA experiment, Taylor et al. 2002), and $n(S) \approx (92 \pm 23)\ (S_{31\ GHz}/1Jy)^{-2.0}$ sr^{-1} Jy^{-1}, for $S_{31\ GHz} > 5$ mJy (from the CBI group, Mason et al. 2002). Apart from these source counts, we can also extrapolate the μJy source counts at 8.4 GHz from VLA observations (Fomalont et al. 2002) up to 30 GHz. Using the spectral index $\alpha = 0.5$ ($S \sim \nu^{-\alpha}$), we obtain

[3] Indeed, this relation holds for all cases where the frequency dependence of the observed flux of the object can be factorised, i.e. $S_\nu = g(\nu)\Phi$, where Φ does not depends on ν.

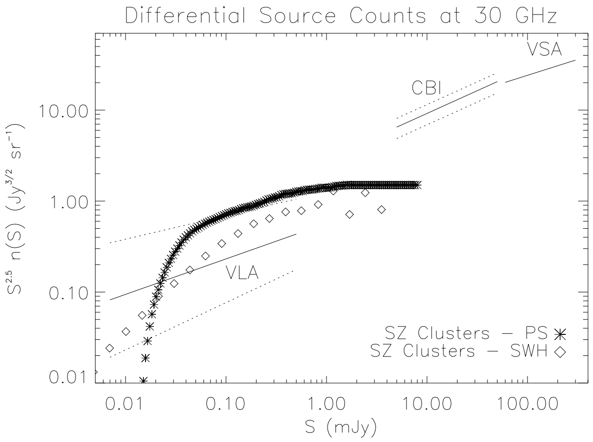

Figure 4. Differential source counts for SZ clusters at 30 GHz, normalised to the Euclidean slope. We show the results from a Press-Schechter prescription with $M_{min} = 5 \times 10^{13} h^{-1} M_{\odot}$ and $\sigma_8 = 0.9$ (see section 7.2 for details), as well as the source counts from the paper of SWH (squares) using hydrodynamic simulations. Both source counts for clusters compare well in shape around 1 mJy, although the hydrodynamic simulations show a ~20% less objects at these fluxes, and do not show an strong cutoff at low fluxes. For comparison, we also present here the differential source counts for radio sources at 30 GHz from several experiment: VSA (Taylor et al. 2002), at 34 GHz; CBI (Mason et al. 2002) at 31 GHz; and VLA (Fomalont et al. 2002) at 8.4 GHz. The source counts for this last experiment have been extrapolated up to 30 GHz using their mean spectral index $\alpha = 0.75$. From the simple observation of these source counts, we expect that experiments with high angular resolution are going to be dominated by radio sources, if they do not consider a source subtraction strategy.

$n(S) \approx (8.4 \pm 0.8)\ (S_{30\ GHz}/1Jy)^{-2.11\pm0.13}$ sr^{-1} Jy^{-1}. All these source counts are summarised in Figure 4.

We should mention that the contribution of radio sources to the power (and thus to the skewness) is decreasing with frequency in power $\nu^{\alpha+2}$, where α is the spectral index of radio sources. Therefore, the contribution of radio sources to the observed map becomes less important at higher frequencies ($\nu \gg 30\ GHz$), while the contribution of clusters does not depend on frequency in the Raileigh-Jeans (RJ) region of the spectrum. It is important to remind that other populations of sources (e.g. thermal dust emission from galaxies) contribute to the source counts at higher frequencies. However, we expect that future experiments like ALMA will show us those populations very precisely.

Given these source counts, the shapes of the corresponding distribution functions are characterised by long positive tails, as we have seen in the previous section. Inclusion of the clustering effects of sources (Barcons 1992) broadens the shape of the $P(D)$, but the important point here is that the long positive tail is still maintained.

4.2 SZ clusters

Korolev, Sunyaev, & Yakubsev (1986) discussed count curves for thermal SZ clusters, and showed that they differ strongly from the case of radio sources. de Luca, Desert, & Puget (1995) have derived the source counts for the thermal SZ effect using the Press-Schechter mass function and assuming unresolved single-type clusters. For the scaling of the temperature with the mass of the cluster, they use $T_e \sim M^{2/3}(1+z)$, so $S_\nu \propto M^{5/3}$. These numbers are in agreement with those obtained from recent X-ray observations (Mohr, Mathiesen, & Evrard 1999; Ettori, De Grandi, & Molendi 2002), and have been shown to fit simultaneously optical and X-ray cluster data (Diego et al. 2001). de Luca, Desert, & Puget (1995) show that typical curves can be well fitted by Euclidean power-laws $n(S) = K|S|^{-2.5}$ down to a few mJy, with typical values of $K \sim 0.44$ sr^{-1} Jy^{-1} (extrapolated down to 30 GHz $\equiv$ 1 cm), and introducing a low-flux cutoff of $S_0 \approx 0.1$ mJy. SWH, using hydrodynamical simulations, came to similar conclusions, although their results do not show an exact power-law behaviour, and the low-flux cutoff is one order of magnitude smaller. For illustration, we show in Figure 4 these source counts, and our derived source counts for PS clusters, together with the radio source counts described in the last subsection. The qualitative behaviour is the same pointed above. These curves will be described in detail in Section 7. Here, we will point out two general aspects of any modelling of SZ clusters.

First, we should stress that the value for S_0 in each model (semi-analytic or numeric) depends on the chosen mass cutoff, M_{min}, i.e. the minimum mass of an object contributing to the SZ effect (see discussion at the end of section 2). This minimum mass (M_{min}) is related to the minimum flux (S_{min}) observed in a given cosmology. Using equation (1), and assuming that the gas in the cluster is isothermal, we obtain the expression for the total SZ decrement S_{tot} for a galaxy cluster, as a function of its mass

$$S_{tot} = \frac{2(kT_{cmb})^3}{(hc)^2} \frac{g(x)\sigma_T}{d_A^2(z)} \frac{kT_e}{m_e c^2} \frac{M f_g}{\mu_e m_p} \qquad (20)$$

where $d_A(z)$ stands for the angular diameter distance, and f_g is the gas mass fraction. Using the scaling $T_e = T_{e0}(M/M_0)^{2/3}(1+z)$ pointed above, we can derive for the Rayleigh-Jeans region of the spectrum that

$$S_{tot}^{RJ} = -1.9 \times 10^5 h^{-1} \frac{f_g}{\mu_e} \left(\frac{\nu}{30\ GHz} \right)^2 \left(\frac{T_{e0}}{9 \times 10^7\ K} \right) \times$$

$$\times \left(\frac{M_0}{10^{15} h^{-1} M_{\odot}} \right) \left(\frac{M}{M_0} \right)^{5/3} (1+z) \left(\frac{1\ Mpc}{d_A(z)} \right)^2 \qquad Jy\ (21)$$

From here, it is straight-forward to infer the minimum flux for a given M_{min}. As an example, if we use the standard values $h = 0.7$, $\Omega_m = 0.3$, $\Omega_\Lambda = 0.7$, and we assume a constant value $f_g = 0.1$, then we find that for a given mass we have the minimum flux at $z \approx 0.98$, and its value is

$$|S_{min}^{RJ}| \approx 20 \left(\frac{M_{min}}{M_0} \right)^{5/3} \qquad mJy$$

at 30 GHz. Typical values for S_{min} can be seen in Table 1. Korolev, Sunyaev, & Yakubsev (1986) were considering T_e independent on redshift, so S_{min} in their case was reached simultaneously with the minimum of angular diameter. Here we use a dependence of T_e with redshift ($\propto (1+z)$), and hence the minimum is reached when the function $(1+z)/d_A^2(z)$ takes its minimum.

Finally, we will mention that the inclusion of large scale

Table 1. Dependence of the observed flux cutoff for clusters with the minimum mass of a cluster, for $\nu = 30$ GHz (see details in text).

M_{min} ($M_\odot$)	$\|S_{min}\|$ (mJy)
10^{14}	0.238
5×10^{13}	0.075
10^{13}	0.005
3×10^{12}	0.0007

clustering in the simulations has been studied by several authors (e.g. Cole & Kaiser 1988; Zhang, Pen & Wang 2002). As we pointed in the last subsection, clustering broadens the shape of the $P(D)$ function respect to the poissonian case. In any case, these studies confirmed that the PDF for y parameter is always characterised by a long positive tail, which corresponds to a negative tail when $\lambda > 1.25$ mm, independently of whether we include clustering or not.

5 CONTRIBUTION OF THERMAL SZ SOURCES TO THE BISPECTRUM OF CMB ANGULAR FLUCTUATIONS

A detailed study of the non-gaussian aspects of the thermal SZ effect can be found in Cooray (2001). Here we will show that the result about the change in sign from the previous section holds for the bispectrum, or indeed any odd-moment of the distribution.

We first decompose the temperature anisotropy in the spherical harmonics basis, so we have $\delta T/T_{cmb}(\hat{n}) = \sum_{\ell m} a_{\ell m} Y_{\ell m}(\hat{n})$. From here, the bispectrum is usually defined as $B_3(\ell_1 m_1, \ell_2 m_2, \ell_3 m_3) =< a_{\ell_1 m_1} a_{\ell_2 m_2} a_{\ell_3 m_3} >$ (e.g Luo 1994). For the case of a thermal SZ sky, the temperature anisotropy will be given by $\delta T/T_{cmb} = \hat{f}(x)y$, where $\hat{f} = x coth(x/2) - 4$. In this equation, all the frequency dependence is factorised in the $\hat{f}(x)$ function. Given that the decomposition in the $Y_{\ell m}$-basis is unique, we can conclude that the $a_{\ell m}^{SZ}$-coefficients will satisfy the relation $a_{\ell m}^{SZ} = \hat{f}(x) y_{\ell m}$, where the $y_{\ell m}$ quantities correspond to the coefficients of the decomposition of the y function. In this way, we can write

$$B_3^{SZ}(\ell_1 m_1, \ell_2 m_2, \ell_3 m_3; \nu) = \left[\frac{\hat{f}(x)}{\hat{f}(x_0)} \right]^3 B_3^{SZ}(\ell_1 m_1, \ell_2 m_2, \ell_3 m_3; \nu_0) \qquad (22)$$

where we explicitly see the change in sign when we pass through $\nu = 217$ GHz. A similar relation also holds for all the higher odd-moments of the $a_{\ell m}^{SZ}$ quantities.

Therefore, we expect an overall change of the sign of the contribution of SZ clusters to the bispectrum when comparing two maps, one observed at $\lambda < 1.25$ mm and the other one at $\lambda > 1.25$ mm. However, for the case of SZ clusters, we would expect a larger value of the non-gaussian features in real space. The reason is that clusters are localised objects in real space, but when averaging modes in Fourier space, the resulting non-gaussianity is diluted. As an illustration of this fact, Zhang, Pen & Wang (2002) show that the kurtosis is (roughly) twice larger in real than in Fourier space when comparing angular scales around $\ell \sim 1000$, while for $\ell \gtrsim 6000$, kurtosis in Fourier space goes rapidly to zero. Hence, it is better for the detection of negative skewness to work directly with real-space statistics, with the advantage that they are easier to infer from data. This approach has been used by several authors, and in particular Cooray (2001) gives the relationship between the bispectrum and the skewness of the map smoothed on some scale with a given window function. The important point here is that this skewness, filtered at some scale, will exhibit the same sign-dependence with frequency.

Summarising these sections, the main characteristics of SZ clusters are the long negative tails of their brightness distributions at frequencies below 217 GHz, the absence of sources in the vicinity of $\lambda = 1.25$ mm, and the existence of a positive contribution at $\lambda < 1.25$ mm. In addition, skewness (or any odd-moment of the map) will retain the net sign of the effect.

6 ESTIMATORS WHICH DISCRIMINATE THE SIGN OF THE SOURCES

In this section, we will be interested in the problem of determining if an excess of power in a map is due to positive of negative source. Therefore, we will not be interested in identifying individual features in the maps, but in an average contribution. As has been pointed out, we will use here the P(D) function. This function, for a given map, can be estimated by selecting a reasonable flux interval ΔD, and computing an *histogram* (number of pixels with a flux between $D - \Delta D/2$ and $D + \Delta D/2$).

Let $P_s(D)$, $P_{SZ}(D)$, $P_{cmb}(D)$, and $P_n(D)$ be the distribution functions for the point sources, the SZ clusters, the CMB and the instrumental (plus atmospheric) noise, respectively. The observed $P(D)$ function will then be given by their convolution,

$$P(D) = P_s(D) \star P_{SZ}(D) \star P_{cmb}(D) \star P_n(D) \qquad (23)$$

The (primordial) CMB distribution function is assumed to be a Gaussian, although for the considered angular scales ($\ell \gtrsim 2000$), it is expected to produce a negligible contribution compared with the SZ or with the noise. We will discuss this point in detail in section 10. The noise is also assumed to be gaussian distributed. This is a reasonable assumption for single dish radio-telescopes, and drift-scan interferometers, but also can be used for CLEANed images of tracking interferometers. Thus, the expected non-gaussianity in the $P(D)$ is introduced by sources (positive or negative), whose distributions are characterised by skewed shapes. Therefore, if we want to detect this asymmetry, and in particular, its sign, one could use one of the following estimators:

• **Asymmetry** (A) of the observed $P(D)$ distribution. This quantity can be estimated directly as the difference in area between the positive and negative regions:

$$A \equiv \int_{D_p}^{+\infty} P(D) dD \; - \; \int_{-\infty}^{D_p} P(D) dD \qquad (24)$$

where D_p stands for the value at which the $P(D)$ function peaks. Previous equation assumes that $P(D)$ is normalised to unit area, i.e. $\int P(D) dD = 1$, so A directly gives the fractional difference in area. It should be noted that D is usually quoted with respect to the deflection around the mean level ($\overline{D}$), so once we have the $P(D)$ function, we make $D \to D - \overline{D}$, with $\overline{D} = \int DP(D)dD$.

• **Non-gaussianity of the wings**. If we obtain the $P(D)$ function, we could test the presence of point sources/SZ clusters even in the case when they produce a mutually cancelling asymmetry. This can be done by comparing the positive/negative tail of the distribution with the one expected from gaussian noise. This excess could be quantified as:

$$\Delta_+ \equiv \int_{D_p}^{+\infty} [P(D) - G(D)]dD \qquad (25)$$

for the positive tail, where G(D) is the expected distribution if we only have noise (normally assumed to be gaussian), and a similar equation for the negative one.

• **Skewness** of the observed map. This cumulant has information about the overall sign of the features producing the deviation from gaussianity. This quantity can be estimated using the third centred moment of the data:

$$E[M_3] = \frac{1}{N_{pix}} \sum_{i=1}^{N_{pix}} (x_i - E[\overline{x}])^3 \qquad (26)$$

where $E[...]$ means that this is an estimator of the quantity inside brackets, N_{pix} is the number of pixels of the map, x_i is the measured flux density at pixel i, and $E[\overline{x}] = \frac{1}{N_{pix}} \sum_i x_i$ is the standard estimator for the mean of the distribution. From here, the skewness is obtained as $Skew \equiv M_3/\sigma^3$, where σ is the rms of the data. Equation (26) is a biased estimator of the third moment of the population, but for large N_{pix} it converges to the true M_3 value. Assuming an underlying gaussian PDF, the variance of this estimator (to lowest order in $1/N_{pix}$) is $Var(E[M_3]) = \frac{6}{N_{pix}} Var(x)^3$ (see Kesden, Cooray & Kamionkowski (2002)).

If the $P(D)$ is known, any moment of the distribution can be derived from it, and in particular, the skewness can be written as

$$Skew = \frac{\int D^3 P(D)dD}{\left(\int D^2 P(D)dD \right)^{3/2}} \qquad (27)$$

• **Bispectrum** of the observed map. We will concentrate here on the quantities $B_\ell \equiv B_{\ell\ell\ell}$, which in the case of statistical isotropy are related to the B_3 function defined above as

$$B_3(\ell_1 m_1, \ell_2 m_2, \ell_3 m_3) = \begin{pmatrix} \ell_1 & \ell_2 & \ell_3 \\ m_1 & m_2 & m_3 \end{pmatrix} B_{\ell_1 \ell_2 \ell_3} \qquad (28)$$

where the (...) is the Wigner $3-j$ symbol. In particular, we will be interested in the dimensionless bispectrum, $I_\ell \equiv B_\ell / C_\ell^{3/2}$ (e.g. Ferreira, Magueijo, & Gorski (1998)). The absolute value of this quantity will be the same for any frequency, while it will change its sign when we are observing above or below $\lambda = 1.25$ mm. A fast and efficient method to compute the angular bispectrum up to $\ell \sim 100$ for maps on the sphere is described in Komatsu et al. (2002), and applied to COBE data. However, for the case of small patches of sky (as is the case for CBI or BIMA), we can use the flat-sky approximation, and the estimator described in Santos et al. (2002).

Any of the above estimators is able to detect an excess of positive unresolved sources over negative ones (or viceversa). However, the study of the $P(D)$ function is preferable to the computation of skewness, given that it contains much more information. Unfortunately, obtaining the $P(D)$ function for sources/clusters from noisy data requires more integration time that just the detection of skewness, as we will see in section 9.

7 SOURCE COUNTS, P(D), SKEWNESS AND BISPECTRUM OF SZ CLUSTERS

P(D) analysis gives much more information than the power spectrum about the sources of CMB fluctuations, and even than skewness or the bispectrum. Therefore, we will describe below the expected P(D) functions, skewness and bispectrum for simulated maps of SZ clusters. It is clear that observers should make a lot of effort to get all the information about P(D), but the results which we will describe here will make it easier to understand our predictions in the following subsections.

In Figure 5 we present the results of simple modelling of SZ thermal effect following the model where "negative" clusters are assumed to have truncated power law source counts and "positive" radio sources have power law source counts up to very low fluxes. In both cases it is possible to compute P(D) numerically from equations in Section 3. For definiteness, we use here $S_0 = 0.1$ mJy, which roughly corresponds to $M_{min} = 5 \times 10^{13} M_\odot$. We are implicitly assuming here that no source subtraction has been carried out on the map, so the width of the P(D) functions is directly related to the source confusion in each case.

We consider here two cases: $\theta_b = 10'$, which is roughly the angular resolution of current experiments (like CBI), and $\theta_b = 1'$, which corresponds to the angular resolution of future experiments dedicated to measure clusters (ACT, AMI, AMIBA, APEX and 8m-South Pole Telescope will have angular resolutions of $1.7'$, $1.5'$, $2'$, $0.8'$and $1.3'$, respectively).

For the beam width $\theta_b = 10'$, the negative sources with truncated source counts produce practically no difference with the P(D) for the "negative" source counts with the same slope extended to zero flux. This is because for this case, the typical flux cutoff is well below the flux which gives the maximum contribution to the P(D). We see immediately that the "positive" radio sources alone have completely different P(D) distribution than "negative" SZ-clusters. For the beam width $\theta_b = 10'$ contribution of positive sources in the total power is larger than the contribution of "negative" SZ clusters, therefore the positive wing of P(D) is similar to the P(D) for sources only. However, the negative wings are very different.

For the beam width $\theta_b = 1'$, the negative tail of the P(D) function of clusters is becoming more important than in the last case. The reason for this dependence is the following: once we have specified the shape of the source counts, and we define the experiment (i.e. we specify θ_b), then the P(D) function is completely defined, and it has the dominant contribution coming from the flux range between the flux at which we have one source per beam area, and the flux at which we expect one source every 30–40 beams. Thus, for smaller beam areas we are sampling lower fluxes where,

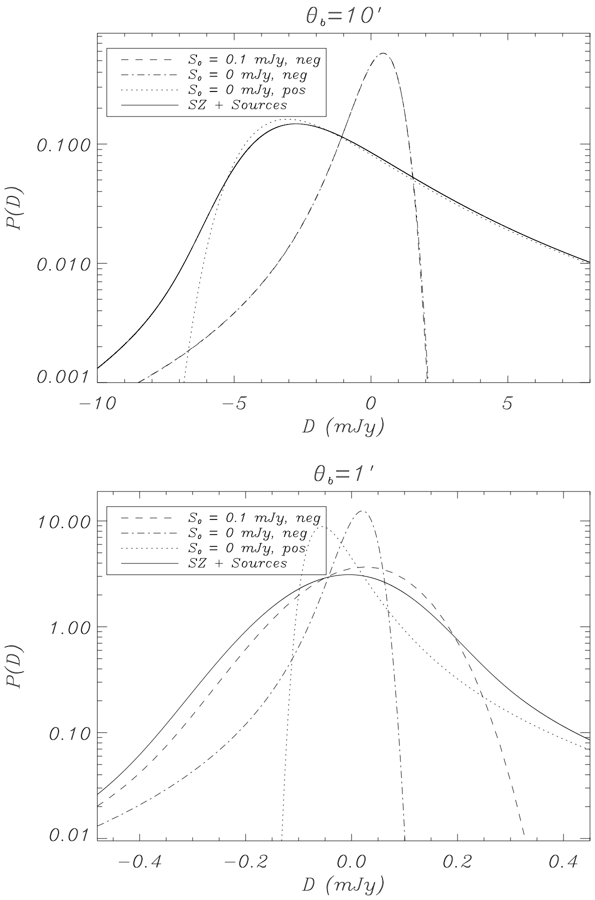

Figure 5. $P(D)$ functions derived from analytical modelling of source counts, for: (a) "negative" sources described with a power-law with parameters $K = 1$ Jy^{-1} sr^{-1}, $\beta = 2.5$, and a low-flux cut-off of $S_0 = 0.1$ mJy (dashed line); (b) same as before, but without considering the cut-off ($S_0 = 0$, dot-dashed line); (c) "positive" sources following a power law with $K = 54$ Jy^{-1} sr^{-1} and $\beta = 2.15$ (dotted lines); (d) sum of the maps of clusters (a) and sources (c), so the P(D) is the convolution of those two cases. The beam is assumed to be gaussian, with a θ_b of $10'$ in the upper panel, and $1'$ in the lower one. The deflection D is refered to $\overline{D}$ in all cases, so all these curves give $\overline{D} = 0$. Comparing cases (a) and (b), we can see the effect of a flux density cut-off on the shape of the $P(D)$ function. A cut-off becomes of importance when we observe a low angular resolution. For these two values of θ_b, the asymmetry introduced by radio sources dominates, because for these values of the spectral indices they are more numerous at a given flux, although for the low value of θ_b (lower panel), clusters increase their relative contribution. However, figure shows that studying the $P(D)$ function provides information of both positive and negative contributions.

according to figure 4, clusters become more numerous compared with radio sources (at a given flux).

We would also mention that if we go deep enough in θ_b, we would reach the low flux cut-off for clusters, and positive sources will dominate again. The existence of a low flux cut-off is clearly seen in the figure for $\theta_b = 1'$, where the shape of the $P(D)$ function is sensitive to the cutoff flux, and thus is completely different from the shape that we would expect if we had no truncation flux. Therefore, we can see that $P(D)$ at these angular resolutions will also give us information about the truncation in flux for SZ clusters, and hence, about the low mass cutoff.

In the following subsections, we will explain in more detail these general aspects by using simulations of SZ clusters, and we will derive the $P(D)$ function from these simulated maps. Through this subsections, we will illustrate the $P(D)$ curves for the angular resolution of $\theta_b = 1'$.

7.1 Modelling clusters using Press-Schechter prescription

Statistical properties of the population of SZ clusters has been extensively studied in the literature (see SWH, fig.4 in that paper, for a recent review). For the case of the power spectrum, the published estimates show differences of an order of magnitude, although these differences can be understood due to the different scaling relations and mass ranges considered in each case. Therefore, we will be interested here in determining the qualitative behaviour of these new quantities ($P(D)$, skewness and bispectrum). For this purpose, we will use a simple modelling of clusters, based on a Press-Schechter prescription. If someone is interested in predictions in agreement with hydrodynamic simulations, then it is possible to use refined versions of the PS formalism, as that described in Sheth & Tormen (1999), or in Jenkins et al. (2001). In PS, the comoving number density of bound objects of total mass M at redshift z, is given by

$$\frac{dn(M,z)}{dM} = -\sqrt{\frac{2}{\pi}}\frac{\overline{\rho}}{M}\frac{d\sigma(M,z)}{dM}\frac{\delta_c}{\sigma^2(M,z)}\exp\left[\frac{-\delta_c^2}{2\sigma^2(M,z)}\right] \quad (29)$$

where $\overline{\rho}$ is the mean comoving background density, $\sigma(M,z)$ is the variance of the linear density fluctuation field filtered on some mass M, $\overline{\rho}$ is the mean comoving background density, and δ_c is the linear density contrast of a perturbation that has virialized.

In our modelling, we will assume the value of $\delta_c = 1.686$ (see e.g. Molnar & Birkinshaw (2000)) and the scaling of $\sigma(M,z)$ with mass from Viana & Liddle (1999). As it was discussed in section 2, it is neccesary to introduce a mass cutoff because dn/dM diverges at low masses. Following Komatsu & Kitayama (1999), we will use $M_{min} = 5\times10^{13}h^{-1}M_\odot$, and $M_{max} = 5\times10^{15}h^{-1}M_\odot$. Changing the upper limit has little effect on the predictions because the PS function falls exponentially. The effect of changing the lower limit is discussed below.

For illustration, we have adopted here the 'concordance' model of Ostriker & Steinhardt (1995), which has $\Omega_{tot} = 1$, with $\Omega_m = 0.3$ and $\Omega_\Lambda = 0.7$, $n = 1$, $h = 0.67$ (where $H_0 = 100h$ km s^{-1} Mpc^{-1}), and the normalisation $\sigma_8 = 0.9$. For the scaling relation of the gas temperature with the mass and the redshift of the cluster, we use the scaling pointed out in section 2, with

$$kT_{gas} = 7.75\left(\frac{M}{10^{15}h^{-1}M_\odot}\right)^{2/3}(1+z)\,keV \quad (30)$$

and we will adopt a β-model for the intra-cluster gas with $\beta = 2/3$. The relationship between the virial radius (r_v) and the core radius (r_c), and their scalings with mass and redshift z are those obtained assuming spherical collapse (see e.g.Atrio-Barandela & Mücket 1999; Molnar & Birkinshaw

2000), and an entropy-driven model with $\epsilon = 0$ for the core evolution (e.g. Bower 1997). The parameters of our cluster model are $r_v(z=0) = 1.3h^{-1}$ Mpc, $r_c(z=0) = 0.13h^{-1}$ Mpc, and $n_c(r=0, z=0) = 2 \times 10^{-3}$ cm^{-3}. In Appendix A we study the dependence of our results on the scaling assumptions, as well as the dependence on the normalisation σ_8.

We then generate 15 realisations of a 1°-side map of SZ clusters using a Press-Schechter law, and a single class of clusters. We have chosen these values to allow direct comparison with the results of of the hydrodynamic simulations of the thermal SZ effect described in SWH[4], which correspond to 15 maps of the same previous size, of the Comptonization parameter y due to structure in the same ΛCDM model between $z = 0$ and $z = 19$. SWH computed the angular power-spectrum of the SZ effect from these maps, as well as the source counts of thermal SZ sources. The mean Comptonization parameter in our 15 Press-Schechter realisations is $< y >= 2.1 \times 10^{-6}$.

7.2 Source counts for clusters following a Press-Schechter prescription

When generating the previous 15 realisations, we keep the total flux of all the simulated clusters, as well as the core and virial radius, so we are able to find out the source counts for our maps. These source counts are presented in figure 6. In the top panel, we show these counts as a function of the flux, for the frequency of 30 GHz. As expected from the result of de Luca, Desert, & Puget (1995), the slope of the source counts at fluxes greater than ~ 1 mJy corresponds to an Euclidean power-law ($\beta = 2.5$). However, the amplitude of our curve is different from theirs. Our source counts are well fitted by $n(S) \approx 1(S/1Jy)^{-2.5}$ sr^{-1} Jy^{-1} at 30 GHz, and by $n(S) \approx 28(S/1Jy)^{-2.5}$ sr^{-1} Jy^{-1} at 150 GHz, while their source counts at 150 GHz is $n(S) \approx 8.6(S/1Jy)^{-2.5}$ sr^{-1} Jy^{-1}. This difference is due to the fact that they introduce an extra normalisation factor in the PS mass function to fit the observed mass function in X-rays, and that changes the total amplitude.

Our prediction for the source counts compares well with that of SWH (open squares), although it is clear that the hydrodynamical simulations do not show an strong cut-off in flux, but they have much more 'small' (low mass) objects. This excess of small objects respect to the PS result will be responsible for a larger power at small angular scales, as it has been discussed in SWH. We can see better this point in the bottom panel of figure 6, where we show the source counts as a function of the angular radius of the cluster. We define here the angular radius as the radius which contains half of the total flux of the cluster. It is interesting to see that if we only consider clusters with a flux density greater than a given value, then the most brightest clusters in the PS maps are the largest ones in size. From this figure, we immediately see that for the angular resolutions of the upcoming SZ experiments ($\theta_b \approx 1'$), more than 90% of the clusters will be unresolved objects (or even more, if we look at the SWH source counts). We would like to stress that

[4] These simulations are quoted in that paper as 134A, and have been corrected for the h factor.

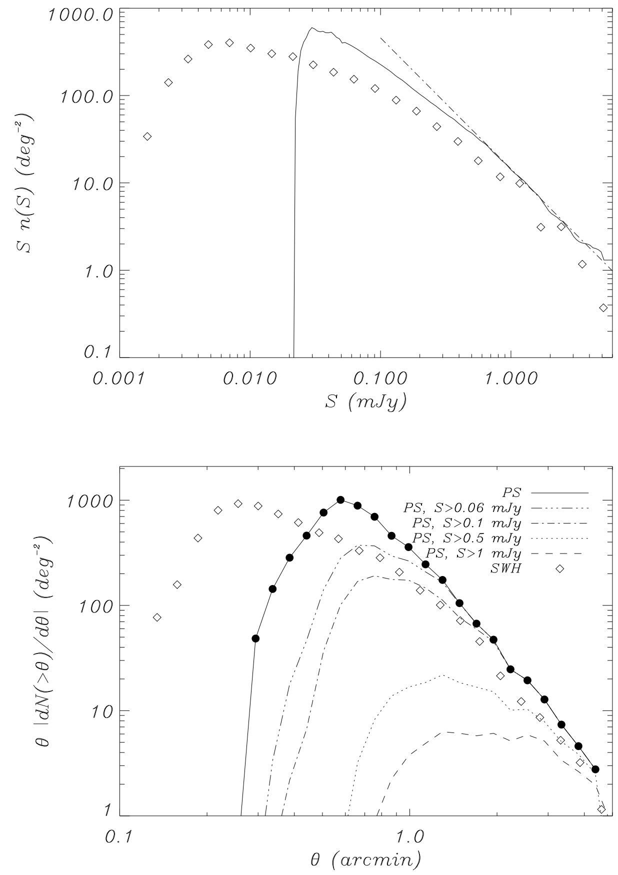

Figure 6. Top: Differential source counts at 30 GHz from the 15 simulated maps following the PS prescription (solid line). As expected, the behaviour at fluxes $S \gtrsim 1$ mJy is well described by a power-law with $\beta = 2.5$, and we have a strong cutoff at low fluxes, corresponding to the mass cutoff $M_{min} = 5 \times 10^{13} h^{-1} M_{\odot}$. In this case, this power law is described by $n(S) \approx 1(S/1Jy)^{-2.5}$ sr^{-1} Jy^{-1}. For comparison, we also show (open squares) the results from SWH. These curves are also presented in Figure 4, in the context of the source counts for radio sources. Bottom: Differential source counts from the 15 maps following a PS prescription, as a function of the source angular radius. We again use the coordinates $|\theta dN/d\theta|$, where we explicitly see the typical size of the most common sources. We present the source counts for the whole dataset (solid circles with solid line), and considering only sources with a flux at 30 GHz greater than a certain threshold. We can see that the most intense sources are also the largest ones. We also include the results from SWH (open squares) showing that the hydrodynamical simulations have a larger amount of small sources, and a wider curve.

the coordinates that we are using to plot the source counts are specially suitable, because they directly give us the total amount of sources at a given angular size/flux interval. In these coordinates, we clearly see that our PS modelling with $M_{min} = 5 \times 10^{13} h^{-1} M_{\odot}$ produces a peak of objects with fluxes around 0.04 mJy and sizes around $0.6'$, and below these quantities we have an strong cutoff (both in size and flux), as expected from the discussion on section 2. It is important to note that for the angular size of $\theta = 0.6'$ (close to the resolution of APEX), we have around ~ 1000 sources per square degree, so given that the number of beam areas

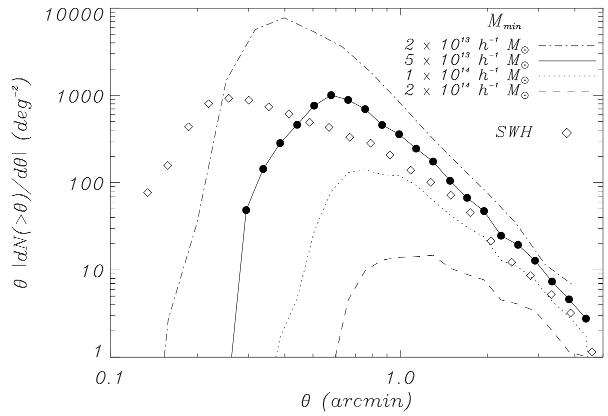

Figure 7. Dependence of the differential source counts (as a function of the source angular radius) with the selected minimum mass for the Press-Schechter mass function. Curves for $M_{min} \geqslant 5 \times 10^{13} h^{-1} M_\odot$ have been obtained from the 15 PS realisations used in figure 6. The curve for $M_{min} = 2 \times 10^{13} h^{-1} M_\odot$ has been derived, just for illustration purposes, from an small realisation of 3 square degrees using this new low mass cutoff. We also show the source counts from SWH.

inside a square degree is $\sim 10^4$ for $\theta_b = 0.6'$, we have that at this angular scale we will obtain 1 source every 10 beams. These values are inside the confusion (e.g. Scheuer (1957)), so the $P(D)$ function is a suitable tool to study them. For larger values of θ_b (e.g. $1.3'$ for the South Pole Telescope, or $\sim 10'$ for present day experiments), we will be even more inside confusion due to these small clusters.

The natural question which follows now is to explore if this conclusion holds for different values of M_{min}. For this purpose, we should study the dependence of the source counts as a function of the angular size using different values for M_{min} in the simulations. This can be done using our simulations by selecting clusters with masses above the new threshold. This is done in figure 7. As we would expect, the θ value at which we have the maximum amount of sources (θ_{peak}) roughly scales as r_v. Fitting our data, we have:

$$\theta_{peak} \approx 0.6' \left(\frac{M_{min}}{5 \times 10^{13} h^{-1} M_\odot} \right)^{1/3}$$

We can also infer from here the total amount of sources (per square degree) that we have at that angular scale (N_{peak}), obtaining

$$N_{peak} \approx 1000 \left(\frac{M_{min}}{5 \times 10^{13} h^{-1} M_\odot} \right)^{-2.8} \qquad deg^{-2}$$

Using these two last equations, we conclude that for the angular resolution θ_{peak}, we expect 1 source every $10 \times (M_{min}/5 \times 10^{13} h^{-1} M_\odot)^{2.13}$, which is smaller than 30 only for $M_{min} < 8.4 \times 10^{13} h^{-1} M_\odot$.

Finally, we can see from figure 7 that all future experiments (with $\theta_b \approx 1'$) will be confusion limited at this angular resolution if $M_{min} \lesssim 1.1 \times 10^{14} h^{-1} M_\odot$. For all of them, a $P(D)$ analysis will be suitable, and in addition, this analysis will provide information about the low mass cutoff.

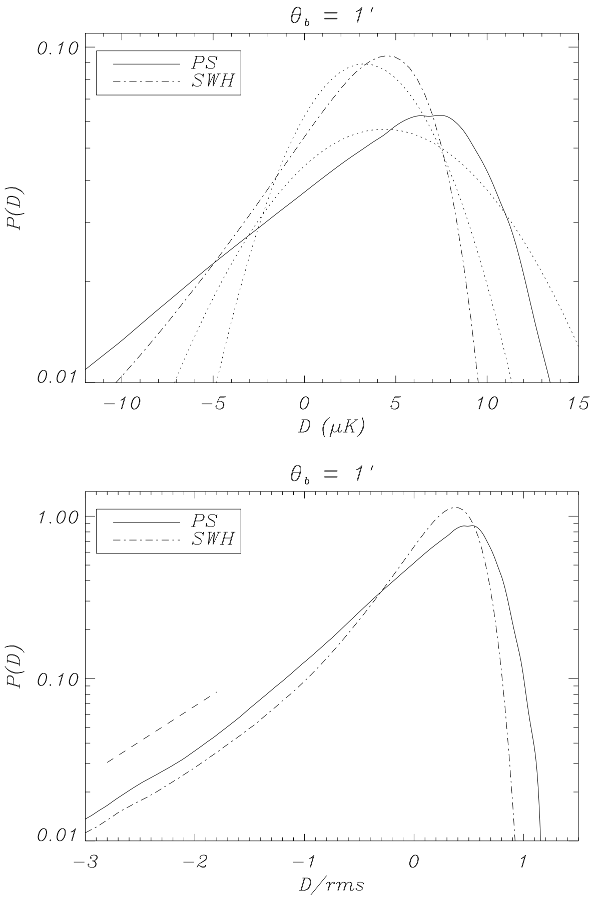

Figure 8. First panel: $P(D)$ function for a single map of SZ clusters following a Press-Schechter prescription (solid line), and for an hydrodynamic simulation from Springel et al. 2001 (dot-dashed line). Both maps are $1°$ on a side, with a pixel size of $0.12'$; they have been smoothed with a gaussian beam of $\theta_b = 1'$, and are given for the Rayleigh-Jeans region of the spectrum. These curves can be transformed into PDF curves for y parameter by the transformation $D = -2yT_{cmb}$, so the $P(y)$ function will exhibit a positive tail. The best gaussian fit for both curves is shown with dotted lines, being their widths $\sigma = 6.1\mu K$ and $\sigma = 3.9\mu K$, respectively. Second panel: same functions but computed dividing the map by the rms prior to the $P(D)$ computation. When rescaling by the rms, both curves show the same qualitative behaviour, with a nearly linear tail in these coordinates (log P(D) vs D). Long dashed line shows a straight line in these coordinates for a slope of unity.

7.3 Predictions of the Press-Schechter approximation for P(D) function, skewness and bispectrum

We will be now interested in obtaining the qualitative behaviour of the $P(D)$ function, the skewness and the bispectrum for SZ clusters following PS mass function. Therefore, and through this section and the next one, we will restrict ourselves to the computed simulations, with $M_{min} = 5 \times 10^{13} h^{-1} M_\odot$.

- **P(D) function**. In figure 8 we present the P(D) analysis of the maps generated in both PS and hydrodynamical simulations using a beam size of $\theta_b = 1'$. Usually, the maps of SZ thermal effect are presented as maps of y-parameter.

However, observers are seeing the brightness distribution on the sky. Therefore, we present deviations on the map for the Rayleigh-Jeans temperature. The temperature in the Rayleigh-Jeans region of the spectrum is connected with the y-parameter by the simple relation $\Delta D = -2yT_{cmb}$ (Zeldovich & Sunyaev 1969), but the P(D) graphs are valid for any frequency: we only need to recompute D and P(D) according to formula (18), but using $\hat{f}$ instead of g. Therefore, our plots for $P(D)$ are easy to convert into PDF for y parameter. This opens the possibility for comparing our results for the PS approximation with those of other authors (e.g. Seljak, Burwell, & Pen (2001)).

The P(D) curves for both PS and hydrodynamic simulations show very broad non gaussian negative wings. To demonstrate this, we are presenting on figure 8a the best fit gaussian curves for both P(D) functions. It should be noted that the width of the best fit gaussian ($\sigma = 6.1\mu$K and $\sigma = 3.9\mu$K, respectively) is smaller than the rms of the maps ($rms(PS) = 13.9\mu$K and $rms(SWH) = 12.0\mu$K), because the fitting reproduces the central part of the curve, while the rms is larger because of the negative tail. If these curves were gaussian, both the rms and the σ value would be the same. The two P(D) curves have sufficient differences, specially in the slope of the negative tail. Both of them fall more rapidly than the gaussian fit, and the PS prescription produces an slightly broader curve (because of the slightly larger rms). We will not discuss these differences in detail because it is well known from previous studies that these two methods are giving significantly different results. However, it's impressive that if we include the 'normalisation' D/rms, dividing the maps by their rms before the $P(D)$ computation, the resulting $P(D)$ curves are similar in shape, showing a practically identical slope in the intermediate asymptotic region (see lower panel on fig. 8).

• **Intermediate asymptotic for the P(D) function**. In a broad region, the normalised P(D) curve could be described by a simple analytical formula: the powerful left wing of the P(D) distribution is close to the straight line in the coordinates we used in our figure ($\log(P(D))$ versus D). Therefore, we see that $P(D) \sim exp(aD)$ in a sufficiently broad region of $-3 < D/rms < 0$. This is an impressive feature of P(D) which might help to identify SZ clusters from the noise of the observed maps, given that this behaviour is completely different from a gaussian. We should stress that both the Press-Schechter approximation and the hydrodynamic simulations produce practically the same "*intermediate asymptotic*". In addition, this 'a' factor has an strong dependence with the normalisation σ_8, as we show in the Appendix A, where we find that $a \sim \sigma_8^{4.5}\theta_b^{-0.2}$. The numerical coefficients for this expression are also shown in that appendix.

It's well known that the $P(D)$ distribution for sources with power law source counts $n(S) = KS^{-\beta}$ gives a simple power law asymptotic $P(D) \sim D^{-\beta}$ for high values of the deflection, because it that case the distribution becomes dominated by strong, well-resolved sources. To look for this asymptotic, we presented the graph of the derivative $d\log(P(D))/d\log(-D)$ versus D/rms in Figure 9. In these coordinates the asymptotic $P(D) \sim D^{-\beta}$ will be the horizontal line with d log (P(D))/ d log(-D) = -2.5. Figure 9 shows that $d\log(P(D))/d\log(-D) \approx aD + B$ in the range $-2.5 < D/rms < 0$, which corresponds exactly to the intermediate asymptotic described above P(D)$\sim$ exp(aD). The limiting value of $-\beta = -2.5$ is reached only for very large deviations.

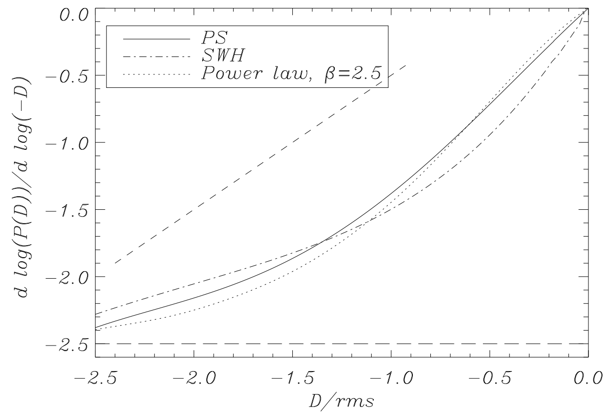

Figure 9. Slope of the negative tail of the $P(D)$ function for SZ clusters following Press-Schechter prescription. It is shown the values for $d\log P(D)/d\log(-D)$, for the average of the 15 realisations of SZ clusters, in the Rayleigh-Jeans region of the spectrum, and using a gaussian beam with $\theta_b = 1'$ (solid line). The dot-dashed line shows the same calculation but for the SWH simulations, while the dotted-line shows the analytic calculation for a power-law source counts with $n(S) = (S/1Jy)^{-2.5}$ sr^{-1} Jy^{-1}. The horizontal axis is plotted in terms of the rms of the map. The slope of this tail tends to the value of -2.5 (horizontal long-dashed line), as expected for a power-law differential source counts with $\beta = 2.5$. However, in this 'intermediate' region, the $P(D)$ curve follows a nearly exponential law ($P(D) \propto \exp(aD/rms)$), with $a \approx 1.0$. This behaviour is completely different from that of a gaussian function.

Finally, it is important to notice that this 'intermediate asymptotic' behaviour can be also obtained semi-analytically, by using a power-law source counts with $\beta =$ 2.5 inside equation (9), as it is also shown in figure 9. Therefore, this intermediate asymptotic is closely related with the PS prescription, which is the ultimate responsible of the Euclidean type power-law behaviour of the source counts for clusters ($N \sim S^{-3/2}$).

• **Skewness**. We investigate the dependence of the skewness introduced by SZ clusters as a function of angular scale, both in real and Fourier spaces. In the real space, to obtain the skewness at a certain scale, we smooth the SZ map using a gaussian filter of FWHM θ_b, and measure the skewness on the smoothed map. The results for modelling using Press-Schechter approximation are shown in Figure 10. Error bars correspond to the field-to-field variance from this ensemble of maps. In the same figure, a dot-dashed line shows the same calculation, but for the hydrodynamic simulations of SWH. It can be seen that the shape of the curve and the values from these two panels are similar for beam sizes larger than $\theta_b \sim 2'$, although for very small angular scales, the hydrodynamical simulations produce a larger skewness, suggesting that it may be even easier to detect. This discrepancy at low angular resolution between PS and hydrodynamical simulations has been already discussed by many authors when predicting the power spectrum, as we discuss in the following item.

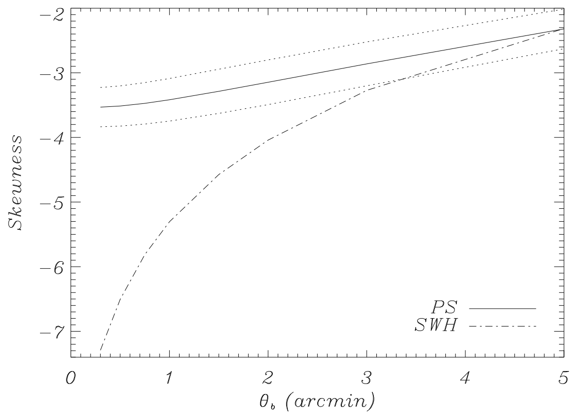

Figure 10. Negative skewness due to SZ clusters as a function of the angular scale. These values have been obtained from 15 (1°-side) simulated maps of the thermal SZ effect using a Press-Schechter prescription (see details in text). For each angular scale, the skewness is obtained after convolving the map with a gaussian beam of FWHM equal to θ_b. The solid line shows the average value of the skewness over these 15 realisations, while dotted lines show the 1-sigma error from this ensemble of maps. The dot-dashed line shows the same result, but obtained from the 15 maps of SWH. The hydrodynamic simulations show an excess of skewness with respect to the PS modelling at small angular scales.

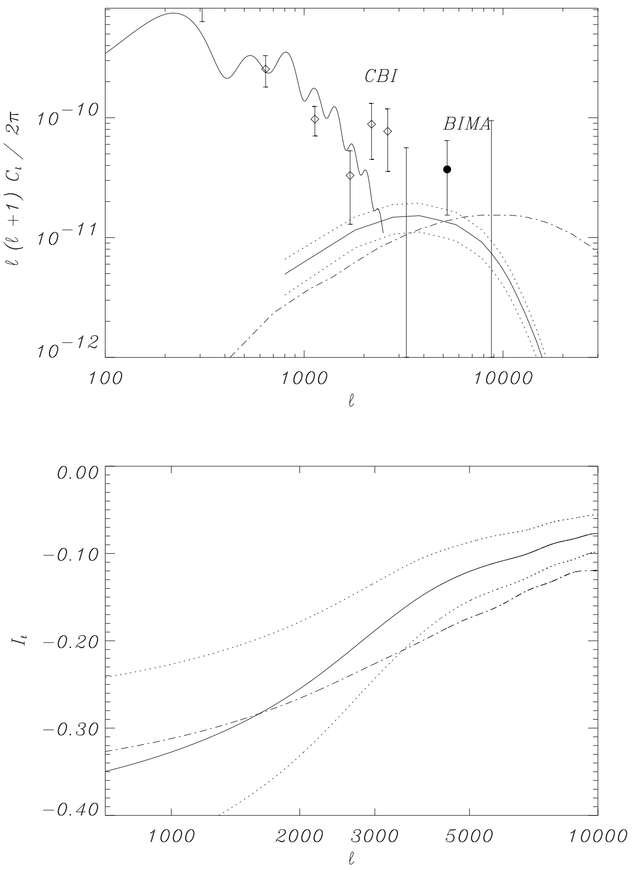

Figure 11. Power spectrum and bispectrum for the thermal SZ effect in the Rayleigh-Jeans region of the spectrum, where the SZ clusters have the same spectrum as the primordial fluctuations (but are negative). First panel: Angular power spectrum (in $(\Delta T/T)^2$ units) for the SZ effect averaged over 15 simulations using the Press-Schechter prescription. Dotted lines shows the 1-sigma field-to-field dispersion. It is also shown a standard ΛCDM model, and the reported measurements of CBI (Mason et al. 2002, open squares), and BIMA (Dawson et al. 2002, filled circles). The dot-dashed line shows the result using the 15 hydrodynamic simulations of SWH. Second panel: Angular bispectrum ($I_\ell = B_\ell/C_\ell^{3/2}$) for the same 15 simulations using PS prescription. Again, the dotted lines shows the 1-sigma field-to-field dispersion, and the dot-dashed line the result using the 15 maps of SWH. As expected, 'skewness' in Fourier space is also negative in this frequency range, but smaller than in real space. Both in the power and in the skewness, the hydrodynamic simulations show an excess of signal (in absolute value) respect to the PS modelling at large ℓ.

• **Bispectrum**. We are presenting the 'skewness' in Fourier space by computing the dimensionless bispectrum (I_ℓ), using the estimator described in Santos et al. (2002). For completeness, we also derive the power spectrum (C_ℓ), although this computation for the case of a Press-Schechter prescription has been done by several authors (e.g. Atrio-Barandela & Mücket 1999; Molnar & Birkinshaw 2000). Here, we explicitly shown that SZ clusters provide a negative contribution to the bispectrum. Similar curves to the ones presented here for the skewness and bispectrum can be found in Cooray (2000). The first panel on Figure 11 shows the power spectrum results for the PS case, in the Rayleigh-Jeans region of the spectrum. To allow comparison, it is also included an standard ΛCDM power spectrum from primordial fluctuations, and the measurements from CBI (Mason et al. (2002)) and BIMA (Dawson et al. (2002)). The dot-dashed line shows the result from SWH, which has a similar amplitude to our PS modelling, although it peaks at larger ℓ with a wider shape. This qualitative behaviour is common to all the hydrodynamical simulations (see SWH for a review of the recent predictions), so they have more power at larger angular scales.

The second panel in Figure 11 shows the angular bispectrum for our PS modelling. As expected, 'skewness' both in real and Fourier space is negative, but the non-gaussianity in Fourier space is smaller than in real space. When comparing our results with those using the SWH simulations, we find again that at small angular scales (high ℓ) the hydrodynamical simulations produce a larger skewness.

8 ROLE OF RADIO SOURCES

We discuss now the influence of radio sources on the observed P(D), skewness and bispectrum. The formalism to describe the confusion noise introduced in a map due to radio sources is widely known, and has been already presented in section 3.2. This formalism is easy to extend to any moment of the observed map, in particular the skewness. Hence, if the population of sources at our observing frequency is described by the differential source counts $n(S) = K(S/1Jy)^{-\beta}$ sr^{-1} Jy^{-1}, then the confusion 'skewness' on our map is given by

$$Skew_c = \frac{< s^3 >}{< s^2 >^{3/2}} = \frac{(3-\beta)^{3/2}}{4-\beta}(K\Omega_e)^{-1/2} s_c^{\frac{\beta-1}{2}} \tag{31}$$

Note that this equation, with a minus sign, is also valid for negative clusters following a power-law source counts. We see that the contribution of radio sources to the skewness will depend on our source subtraction threshold, s_c, i.e. on the most brightest sources remaining in the map. In order to distinguish the signal coming from SZ clusters, it is necessary to decrease these quantities below the level of the SZ signal.

It is obvious that when adding two maps (sources and SZ clusters in this case), both the power ($< D^2 >$) and the third-moment ($< D^3 >$) of the resulting distribution are the sum of the individual quantities, *assuming uncorrelated maps*. Let σ_1 and σ_2 be the rms (power) of each of these two families of sources, and let $Skew_1$ and $Skew_2$ be the (dimensionless) skewness for each one of them. The rms of the combined map is $\sqrt{\sigma_1^2 + \sigma_2^2}$, and the skewness is

$$Skew \equiv \frac{(Skew_1)\ \sigma_1^3 + (Skew_2)\ \sigma_2^3}{(\sigma_1^2 + \sigma_2^2)^{3/2}} \tag{32}$$

Combining these two last equations, we can infer the required flux threshold for the source subtraction in order to have an overall negative skewness in a map containing sources and clusters. However, it is also well-known that using a single map we are unable to subtract sources down to an arbitrary flux level, because of the intrinsic confusion noise introduced by sources. As we have seen in section 3, the minimum subtraction threshold is usually taken to be $s_c = q\sigma_c$, with $q = 3-5$. Inserting this condition in equation (31), we have

$$Skew = q(3-\beta)/(4-\beta) \tag{33}$$

Using $q = 5$ in this equation, and in the equation for the confusion noise (15), we obtain the minimum contribution of radio-sources to any experiment which does not consider any source subtraction strategy. In the particular case of $\beta \sim 2$, which is the case for the observed radio sources at 30 GHz, we have $Skew = q/2$, so the minimum skewness due to sources that we expect without source subtraction is $\sim 1.5 - 2.5$ for $q = 3-5$, and the minimum confusion noise

$$\sigma_c = 2.86(q/3)(K/90Jy^{-1}sr^{-1})(\theta_b/10')^2 mJy$$

If we now convert this into temperature using the Rayleigh-Jeans approximation, we obtain

$$\sigma_c = 10.8(q/3)(K_{30GHz}/90Jy^{-1}sr^{-1})(\nu/30GHz)^{-2}\mu K$$

which is independent of the beam size because $\beta = 2$. Observing at a single frequency and with a single instrument, allows us to go down to q=3 at the most. If we want to go deeper, we need to use information from an instrument with a better angular resolution to decrease the effective value of q, as we see from equation (15).

We illustrate in figure 12 how a source subtraction technique affects the observed $P(D)$ function of a map containing sources and SZ clusters. Radio sources are modelled here with a power-law source counts with parameters $K = 92$ Jy^{-1} sr^{-1} and $\beta = 2$. We have considered different source subtraction thresholds, parameterised in terms of $m \times \sigma_c(q = 5)$. Without source subtraction at all, we can not decrease m below 5. The main result is that, as we would expect, for small values of m we delete the strong positive

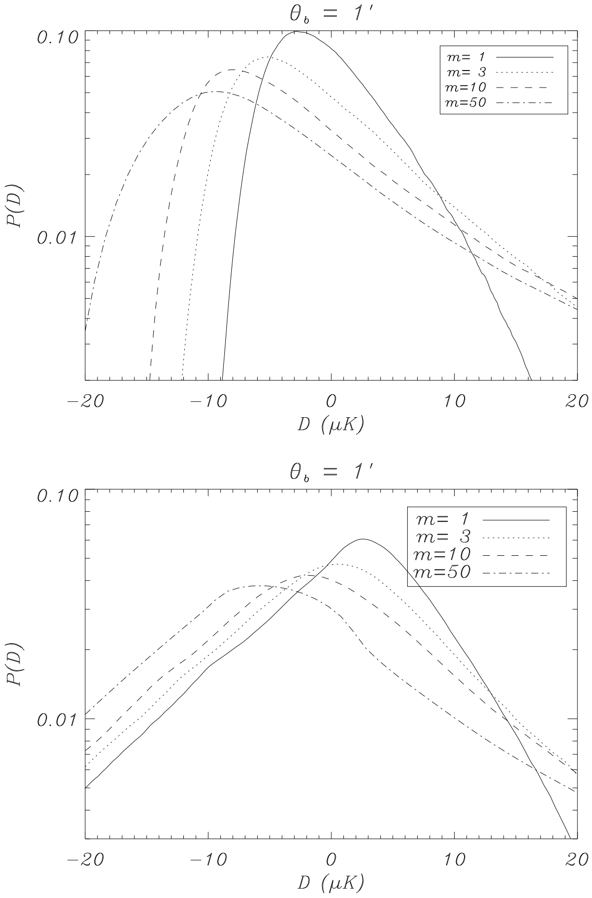

Figure 12. Top: Effect of the source subtraction on the P(D) function of sources. We parameterise the source subtraction limit as $s_c = m\ \sigma_c(q = 5)$, where $\sigma_c(q = 5) = 16.6\mu K$ in this particular case. Here, we consider the following values for m: 1, 3, 10 and 50. All these calculations correspond to radio sources described by parameters $K = 92$ sr^{-1} Jy^{-1} and $\beta = 2$, and using a gaussian beam of $\theta_b = 1'$. Bottom: Same as in the top panel, but adding a realisation of SZ clusters following a PS prescription. In all cases the negative tail is visible, but the asymmetry and the skewness are positive for m values greater than 3, so the detection of the SZ component will require a $P(D)$ analysis if we do not consider a source subtraction strategy. Simply measuring the skewness is not enough to see the negative contribution.

deviations, so $P(D)$ becomes more narrow and permits to look for a negative tail connected with SZ clusters. In particular, we see that the negative tail is always visible, but the asymmetry and the skewness are positive for $m > 3$, so a simple analysis of the skewness will not be able to detect a negative contribution if we do not subtract radio sources from the map.

We will now discuss how this picture changes with the observing frequency and the beam size, assuming that we do not subtract sources at all, so their contribution will be at least $q = 5$ (i.e. $s_c = 5\sigma_c(q = 5)$). We present in figure 13 the P(D) function for the 15 PS realisations, with and without adding to the maps a simulation of sources with $K = 92$ Jy^{-1} sr^{-1} and $\beta = 2$. Just for illustration, it is also computed the P(D) function extrapolating the radio sources up to 100 GHz using $\alpha = 0.5$. As it has been pointed out above,

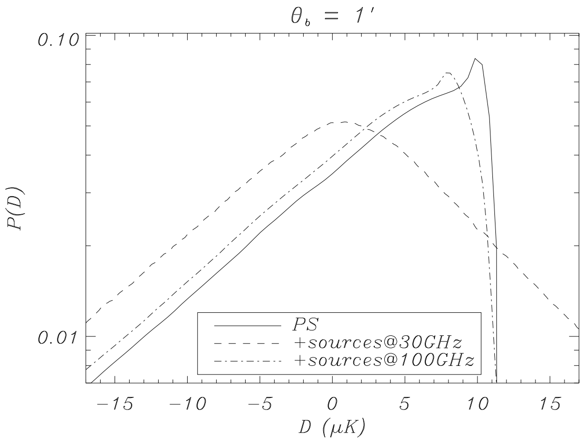

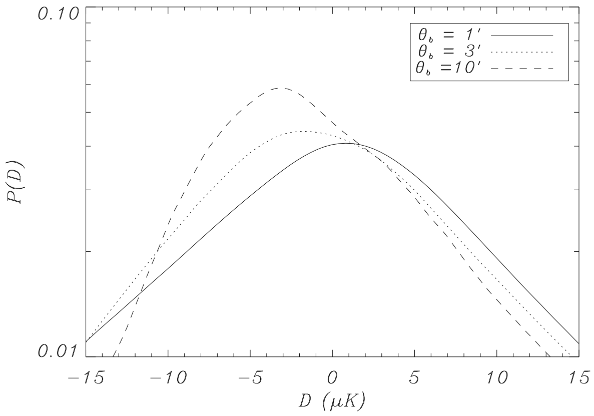

Figure 13. Top: P(D) function for the 15 (1°-side) PS realisations plus sources, assuming that we are able to subtract radio sources down to $s_c = 5\sigma_c (q = 5)$. We calculate sources using the parameters $K = 92$ sr^{-1} Jy^{-1} and $\beta = 2$, and we present the results both at 30 GHz and at 100 GHz. The extrapolation of radio sources up to 100 GHz has been done using an spectral index $\alpha = 0.5$. We can see that, without a source subtraction strategy, radio sources become of the same importance as, or even much more important than clusters at this angular scale for $\nu = 30\ GHz$, while they practically disappear at 100 GHz. Bottom: P(D) function for clusters and sources as a function of the beam size. We use the 15 PS realisations, plus sources as in the top panel, and we compute the P(D) function at 30 GHz. As expected from the simple inspection of figure 4, at larger beam sizes sources are more numerous, so their tail dominates the asymmetry. At smaller beam sizes, clusters become of importance.

at higher frequencies we would expect other populations of sources, so the real $P(D)$ function might show a bigger positive wing. We can see that at these angular scales ($\theta_b = 1'$), and without a source subtraction strategy, clusters can be (at the most) of the same importance of radio sources at 30 GHz. This fact is well-known, and several planned experiments that will operate close to these frequencies (30 GHz) also have designed a source subtraction strategy to eliminate the radio source confusion (e.g. AMI, (Kneissl et al. 2001)).

In the bottom panel of figure 13 we illustrate the dependence of the shape of the $P(D)$ as a function of the beam size (θ_b). As we would expected from the simple inspection of figure 4, and as we pointed out at the beginning of section 7 (see figure 5), at larger beam sizes radio sources are more numerous than clusters, so their tail dominates the asymmetry. At smaller beam sizes, clusters become of importance.

It is important to note here that all these calculations have been done assuming uncorrelated sources, but in principle one could have two types of correlations: spatial correlations between sources (SZ clusters) themselves, and correlations between the positions of the SZ clusters and the radio sources. In the first case, spatial correlations of sources/clusters can be modelled to first order (Barcons 1992) as an extra convolution with another gaussian. Thus, the above tools can still be applied, although it will required a much more detailed study. On the other hand, it is well-known that clusters of galaxies may contain radio point sources (e.g. Birkinshaw 1999; Cooray et al. 1998), so the signal from SZ clusters could be diluted (Holder 2002b; Lin, Chiueh, & Wu 2002). This point can be easily checked by introducing spatial correlations between clusters and radio sources. In the most unfavourable case of having a radio source inside each cluster, we obtain from the previous simulations that skewness is underestimated by about ~ 20 %. This number is in agreement with the result obtained by Holder (2002b), who showed that the rms fluctuations of the thermal SZ effect could be underestimated due to correlations between clusters and radio sources by as much as 30% at the observing frequency of 30 GHz and $\ell \gtrsim 1000$.

9 DETECTION OF A NEGATIVE CONTRIBUTION OF CLUSTERS

The performance of the estimators described on section 6 for detecting a negative contribution of clusters depends on the particular shape of the source counts for both radio sources and SZ clusters. In this subsection, we will concentrate on showing that the skewness may be used to distinguish the nature of the subjacent fluctuations, using for that purpose a toy-model for sources and clusters. Once we are able to detect skewness in the map, the $P(D)$ function will show an asymmetry. However, the determination of the $P(D)$ function of the underlying sources will require additional observational effort than simply measuring the skewness. Thus, the skewness will give us the minimum signal-to-noise level required to distinguish between clusters and radio sources.

We illustrate these facts by computing the $P(D)$ functions and the skewness for the complete set of 15 SZ maps based on PS modelling, observed with a gaussian beam of $\theta_b = 1'$, and adding different noise levels per pixel ($\equiv \sigma_{noise}$), quoted in terms of the power due to clusters (σ_{SZ}). When then consider the following cases for $\sigma_{noise}/\sigma_{SZ}$: 0.3, 1, 2, 5, 10 and 20. We will also assume that the noise is gaussian and uncorrelated, as a first approximation. The resulting P(D) curves are shown in figure 14, while the measured rms in the map, the recovered excess of power, and the observed skewness, are quoted in Table 2. We can see that the tail of the P(D) function has practically disappeared at $\sigma_{noise}/\sigma_{SZ} = 5$, although is still possible to measure skewness in the map at a high significance. When we go to $\sigma_{noise}/\sigma_{SZ} = 10$, the skewness is no longer visible, although it is possible to detect an excess of power. At $\sigma_{noise}/\sigma_{SZ} = 20$, anything can be detected.

If we now include sources in our maps, the determination of how deep we need to integrate in order to get

Table 2. Detectability of the skewness when adding white gaussian noise to SZ maps.

$\sigma_{noise}/\sigma_{SZ}$	rms (μK)	$E[\sigma_{SZ}]$ (μK)	$E[Skew]$	σ_{Skew}
0.3	15.10	14.46	-3.320	0.003
1.0	20.43	14.44	-1.340	0.003
2.0	32.32	14.43	-0.340	0.003
5.0	73.67	14.15	-0.030	0.003
10.0	145.35	14.84	-0.001	0.003
20.0	289.78	18.67	0.0004	0.003

We consider an SZ simulated map following PS prescription, covering 3 square degrees with a pixel size of $0.12'$ and a beam size of $\theta_b = 1'$, with $\sigma_{SZ} = 14.46\mu K$, and we add different noise levels. The obtained P(D) are shown in Figure 14, while we present here the observed power (rms) in the map, the infered signal due to SZ (estimated as $E[\sigma_{SZ}] = \sqrt{rms^2 - \sigma^2_{noise}}$), and the measured skewness in the map (without applying any filtering technique), with its variance (σ_{Skew}).

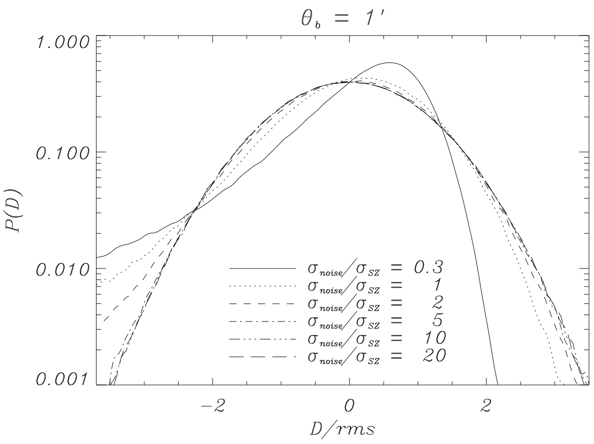

Figure 14. Shape of the P(D) function for clusters when adding instrumental gaussian white noise. A single map of 3 square degrees of SZ clusters following PS prescription has been used, with $\sigma_{SZ} = 14.46\ \mu K$. We add to this map several realizations of white gaussian noise, with the amplitude quoted in the figure, and then we compute the P(D) function. The measured excess of power and skewness in each particular case are quoted in Table 2.

information about the skewness can be done in the following simple way. We define here the signal-to-noise ratio per pixel, S/N, as the quotient $\sigma_{signal}/\sigma_{noise}$. We quote this quantity because it is easy to infer from the map. In addition, it is also straight-forward to convert these values into integration time t for a given experiment, because we usually have $\sigma_{noise} \propto \sqrt{t}$. In the previous expression, σ_{signal} corresponds to the power introduced by clusters and sources all together. Then, if we want a q-sigma detection of skewness, it is straight-forward to derive from equation (32) that we need a signal-to-noise ratio better than

$$\left(\frac{S}{N}\right) \geqslant \left[\left(\frac{Skew^2 N_{pix}}{6q^2}\right)^{1/3} - 1\right]^{-1/2} \tag{34}$$

where $Skew$ is the combined skewness of sources and clusters (32), and N_{pix} is the number of pixels in the map, i.e. $N_{pix} = 4\pi f_{sky}/\Omega_p$, with f_{sky} the fraction of sky covered, and Ω_p the pixel solid angle. For the typical values of skewness found in our simulations, the required signal-to-noise ratio for the detection of skewness due to both point sources and SZ clusters is around 25-40% times larger than the required ratio for the detection of an excess of power. In other words, we need (the well-known result of) 1.5-2 times more integration time to detect skewness than to detect an excess of power.

We will mention here that these values have been obtained directly from the maps, without applying any filtering. These numbers can be improved if we apply to our maps an appropriate filter to enhance the contribution of sources over the noise level, previously to the skewness or P(D) computation. We will discuss this issue in the next section, where we also consider the effect of primary anisotropies on the maps.

10 INCLUDING PRIMARY ANISOTROPIES

The computations in the last two sections were done assuming that the primordial CMB gives a negligible contribution compared with that of the SZ signal and the noise. However, this is only true at arcminute scales, where the primordial anisotropy is damped to very small amplitudes, well-below the level of the expected SZ anisotropy (see the top panel of figure 11). Therefore, only those experiments which are observing at the high multipole region of the angular power spectrum are going to directly observe the cluster contribution. This is the case of interferometers with long baselines (e.g. AMIBA, see Zhang, Pen & Wang 2002, or BIMA (Dawson et al. 2002), which has a primary beam of $6.6'$), or experiments with small fields of view. As it is well-known, if we are observing small patches on sky, we are sensible to multipoles greater than $\ell_{min} \approx 2\pi/\theta_{map}$, being θ_{map} the size of our map (see e.g. Hobson & Magueijo (1996) for a detailed study). Therefore, for small fields of view we are implicitly filtering out the lowest multipoles, and we can directly apply the formalism described in the last section.

However, if our experiment is sensitive to low multipoles ($\ell \lesssim 2000$), then it is necessary to add a new step in our pipeline, which consists in filtering these low multipoles, if we want to remove the contribution of primordial anisotropies. This will be the case for experiments which will cover thousands of square degrees in sky (e.g. 8m South Pole telescope), or experiments covering the whole sky (e.g PLANCK satellite). This step is common to all techniques which are aimed to extract sources/clusters from a map using a single frequency observation. Many filters can be found in literature, going from matched filters (e.g. Haehnelt & Tegmark (1996); Tegmark & de Oliveira-Costa (1998)), pseudo-filters (e.g. Sanz, Herranz, & Martínez-Gónzalez (2001)) or wavelets (e.g. Cayón et al. (2000)). Any of these methods can be used to pre-process the maps, reducing the relative contribution of primary anisotropies, and also that of the noise. The important point is that under linear filters, gaussian data will still be gaussian, and a distribution of sources still will show an skewed shape.

10.1 Effect of primary anisotropies on the observed P(D)

For illustrating this issue, we have performed a new simulation of SZ clusters, covering a larger area (2048×2048 pixels of $0.5'$side each, so the map covers $\sim$ 291 square degrees), using the same parameters as for the previous simulations, but with $M_{min} = 10^{14} M_{\odot}$. The reason of considering such a large area is because future experiments will cover hundreds (or thousands) of square degrees on sky. We add to this map a CMB realisation following the power-spectra plotted in the top panel of figure 11. The rms of the simulated SZ map and the CMB realisation are $5.7\mu K$ and $112.3\mu K$, respectively. Finally, we also add white gaussian noise with an amplitude $10\mu K$ (per pixel of $0.5'$), and we smooth the resulting map with a gaussian beam of $\theta_b = 1'$. Using this map, we have examined two different filters:

- a Hanning (or high-pass) filter, which removes the contribution of all multipoles below a certain value ℓ_0, but linearly increasing from 0 to 1 in the range $[\ell_0 - \Delta\ell, \ell_0 + \Delta\ell]$ to avoid the ringing associated to a sharp cut. We have used here $\ell_0 = 2000$, and $\Delta\ell = 50$.
- a matched filter optimised to detect point-source like objects (Haehnelt & Tegmark 1996), so $W_\ell \propto (B_\ell C_\ell^{TOT})^{-1}$. Here, W_ℓ and B_ℓ are the coefficients in a Legendre polynomial expansion of the filter and of the beam, respectively, and C_ℓ^{TOT} is the sum of the power spectrum of the components to be removed (noise and CMB in this case).

In Figure 15 we show the predicted $P(D)$ function from our simulation when adding CMB primary anisotropies, with and without noise, and the predicted $P(D)$ after filtering the maps with the previous filters. For comparison, it is also shown the $P(D)$ function for the SZ map alone. In order to use the same scale for plotting all the curves, we have divided each map by its rms prior to the $P(D)$ computation. We can see that a simple high-pass filter is able to remove the main contribution from the primordial CMB, so the $P(D)$ function becomes dominated by the contribution of SZ clusters, and the negative tail is visible. However, an small residual signal of the CMB fluctuations still persists, even in the case where we do not consider noise. Nevertheless, this residual can be modelled as an extra gaussian noise: a $P(D)$ analysis does not distinguish two signals if both of them are gaussian. When using the optimal filter, the $P(D)$ function shows its tail more clearly. Therefore, when pre-processing our maps with a filter, we are able to reduce the problem to the case discussed in the previous section, where we only have SZ signal, sources and noise, and hence the negative tail is showing us the presence of clusters. For completeness, we report the number of pixels which are above 3 sigmas in these maps, to illustrate the significance of the "detection" of the tail. For the case which includes noise, these numbers are 7500, 21503, 40475 and 76345 for the non-filtered, the Hanning filtered, the optimal filtered and the pure SZ maps, respectively. These numbers have a sampling error of 106 pixels. For a gaussian distribution, we should expect to have 11324 pixels (0.27% for 3σ) out of 2048^2 in total.

It is also interesting to demonstrate what we would expect if a given survey is covering an small area on sky, but large enough to have an important contribution from primary anisotropies. This would be the case of an hypothetic

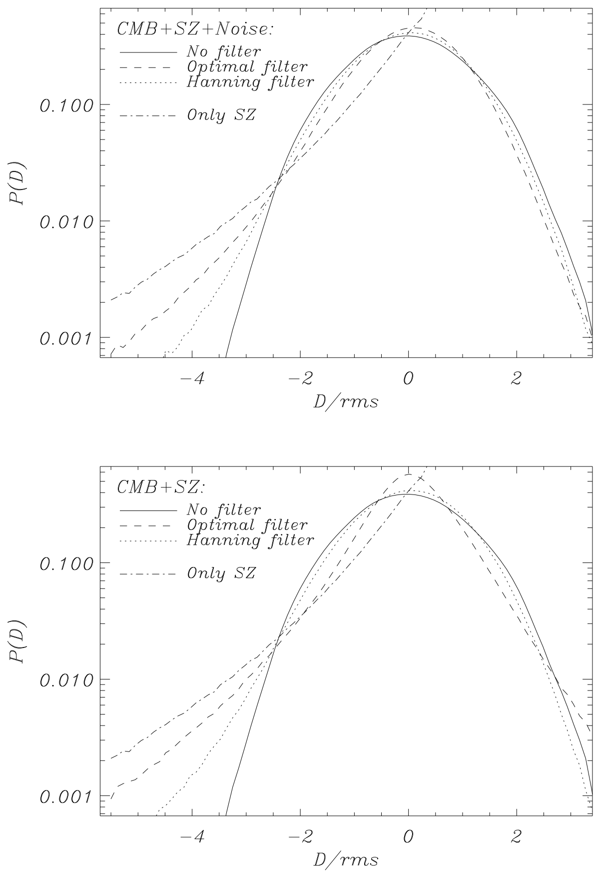

Figure 15. Top: P(D) function from a Press-Schechter SZ realisation of a 291 square degrees patch of the sky, observed with a gaussian beam of $\theta_b = 1'$, for four cases: (a) adding CMB primary anisotropies, and white gaussian noise of 10 μK per pixel (solid line); (b) filtering the previous map with the optimal matched-filter described in Haehnelt & Tegmark (1996) (dashed line); (c) filtering the map with a Hanning (high-pass) filter (dotted line); (d) considering the SZ map alone (dot-dashed line). Bottom: Same as the previous panel, but without including noise. In order to use the same scale for plotting all curves, we have divided each map for its rms prior to the P(D) computation. In this case, $rms(SZ) = 4.9\mu K$, $rms(SZ+CMB) = 112.2\mu K$ and $rms(SZ+CMB+Noise) = 112.3\mu K$.

experiment covering 1°-side patch on sky, so we have used here the simulations described in section 7.1. In this case, we have the additional problem of the sample variance: the observed P(D) function will show deviations from the expected gaussian curve. Therefore, filtering in this case is absolutely necessary. We illustrate this point with figure 16, where we show the P(D) function from a single 1°-side map, containing SZ signal, CMB and no noise, and also the same plot for the average of 15 maps of the same type. We can see that, although the P(D) function for the map without filtering is marginally showing a negative tail when we average 15 maps, the sample variance is completely deleting this tail when we consider a single map. This point can also be illustrated if we use those 15 1°-side simulations to compute the uncertainty introduced by the sample variance in the number of pixels above the 3σ threshold. This number was

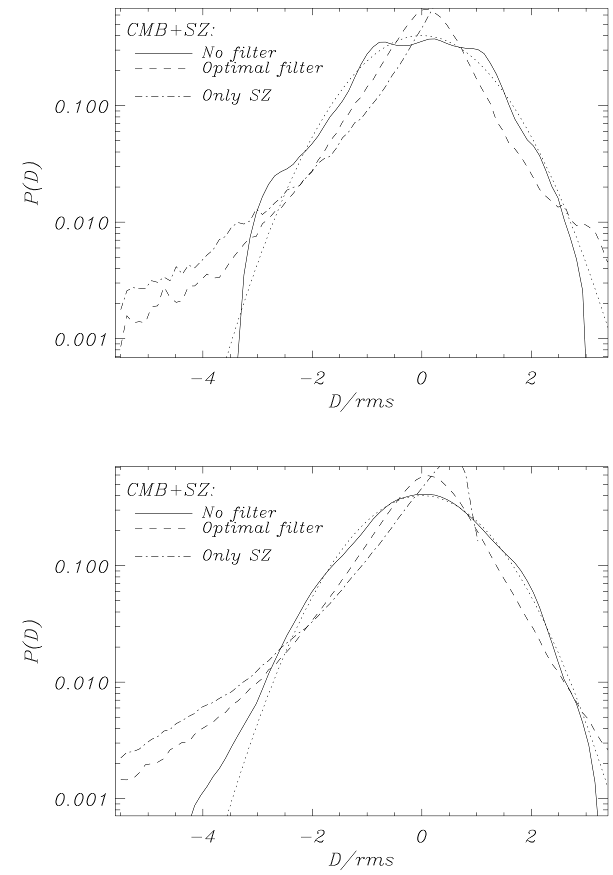

Figure 16. Effect of the CMB sample variance in the observed P(D) function. Top: P(D) function from a single Press-Schechter SZ map of 1°-side, observed with a gaussian beam of $\theta_b = 1'$, for the cases (a), (b) and (d) discussed in figure 15. We can see that the observed P(D) function is distorted due to the sample variance contribution of the primordial CMB anisotropies. The dotted line corresponds to a gaussian with a width equal to the observed rms in the map, i.e. the P(D) function that we would observe if all the signals in the map were gaussian and we had no sample variance. Bottom: same as previous panel, but averaging 15 realisations. In this case, the sample variance is reduced and a negative tail is marginally detected even without filtering. In this case, $rms(SZ) = 12.3\mu K$ and $rms(SZ+CMB) = 54.5\mu K$ in the top panel and $rms(SZ) = 13.9\mu K$ and $rms(SZ+CMB) = 74.2\mu K$ in the bottom one.

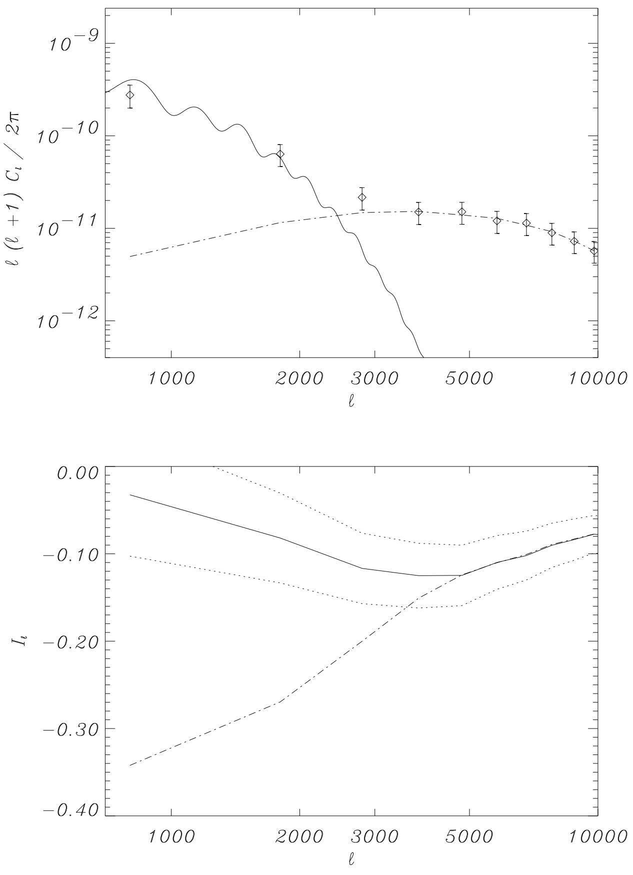

Figure 17. Effect of primordial CMB anisotropies on the observed power spectrum/bispectrum. We use the same 15 realisations as in figure 11, but adding a CMB realisations to each one of them, following the plotted ΛCDM model. Here we do not apply any filtering to the maps. Top: The recovered power spectrum from the 15 realisations (diamonds). Error bars correspond to the field-to-field variance. At low ℓ-values, the power spectrum traces that of the CMB, while in the high ℓ region, the spectrum traces that of the SZ maps (dot-dashed line). Bottom: Bispectrum for the same 15 realisations (solid line). Dotted lines show the 1-sigma field-to-field variance. We see that at high ℓ, the bispectrum follows that of the SZ signal (dot-dashed line), but a low-ℓ (large scales) its goes to zero because the power becomes dominated by that of the primordial CMB, which has zero skewness.

found to be 0.5%, whilst the expected number of pixels for a gaussian distribution above 3σ is 0.27%. However, even in this case the filtering is able to remove the main contribution of the primary anisotropies, and hence the negative tail is seen.

10.2 Effect of primary anisotropies on the observed skewness/bispectrum

We conclude this section showing the expected skewness and bispectrum from our 15 PS simulations taking into account a CMB component in the maps. It is important to notice here that for the bispectrum is not necessary to use any filter, because it directly gives the 'skewness' at each angular scale. These results for the power-spectrum and the bispectrum are shown in figure 17. From here, we can conclude that if the relative contribution of SZ clusters to the observed bispectrum is larger than the one from radio sources, then we expect to directly see their negative signal in the bispectrum without pre-processing the maps.

To obtain the skewness in real-space, we proceed as in section 7.3, but pre-processing the maps with any of the filters described in the last subsection. The obtained results from averaging over the same 15 PS maps are shown in figure 18. The main conclusion is that the residual CMB power in the filtered map is diluting the SZ skewness, although it is still clearly seen. This is exactly what we would expect, using equation (32). From simple inspection of the top panel of figure 17, we expect to have a residual CMB power after

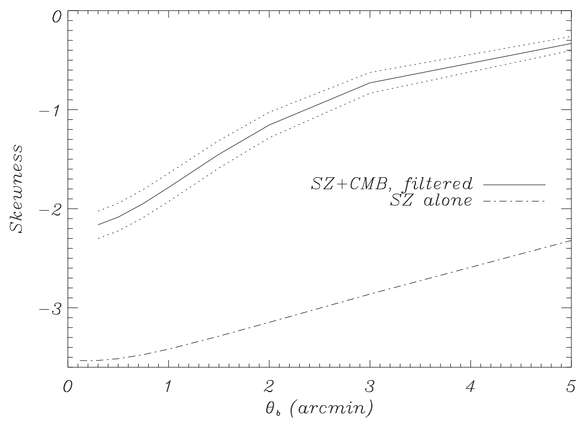

Figure 18. Negative skewness for SZ clusters in the presence of primary CMB anisotropies, as a function of the angular scale. We present the skewness from the same 15 PS maps as in figure 10, with (solid) and without (dot-dashed) adding primordial CMB anisotropies. When the CMB is added, the maps are filtered, prior to the skewness computation, using a Hanning filter with $\ell_0 = 2000$, as described in the text. Although the skewness in real map is diluted due to the residual power from the CMB in the filtered map, it is still detectable.

filtering with a Hanning filter of $\ell_0 = 2000$ which is similar, or slightly smaller than the SZ power. Therefore, we would expect the skewness to be reduced (roughly) by a factor $2^{3/2} \approx 2.8$, as we observed from the simulations.

11 CONCLUSIONS

In this paper we have discussed five statements:

- The contribution of SZ clusters to the map noise at $\lambda > 1.25$ mm does not depend on the wavelength, and has a strong and peculiar non-gaussian negative tail in the $P(D)$ function.
- This contribution has characteristic negative skewness (or bispectrum) at $\lambda > 1.25$ mm. This fact can be used by current single-frequency experiments, such as CBI or BIMA, or by future experiments, such as ACT, AMI, AMIBA, APEX, or the 8-m South Pole telescope, to distinguish if the detected excess of power at small angular scales is due to SZ clusters. In addition, the detection of skewness only requires a factor 1.5 or 2 more integration time than the detection of an excess of power. Once the skewness is detected, the $P(D)$ function starts to show an asymmetry.
- Any multi-frequency experiment would have noise due to clusters of galaxies with $P(D)$ at $\lambda < 1.25$ mm equal to $P(-D)$ at $\lambda > 1.25$ mm.
- Skewness and bispectrum will have different signs in these two spectral regions.
- When dealing with real maps where primordial CMB fluctuations are present, it is necessary to use filters to remove the contribution of large angular scales. Only in that case we can detect the presence of clusters/sources in the $P(D)$ function.

ACKNOWLEDGMENTS

We would like to thank Volker Springel for permission to use the maps obtained in Springel, White, & Hernquist (2001). We also thank S.D.M. White, C. Hernández-Monteagudo, A. Banday, M. Bartelmann, S. Zaroubi and P. Carreira for useful comments. JARM acknowledges support from the CMB-Net European Network. We would like to thank also the anonymous referee for his suggestion of including a discussion about the P(D) function in the presence of primary CMB anisotropies.

REFERENCES

Atrio-Barandela, F. & Mücket, J. P. 1999, ApJ, 515, 465
Barcons, X. 1992, ApJ, 396, 460
Banday, A. J., Gorski, K. M., Bennett, C. L., Hinshaw, G., Kogut, A., & Smoot, G. F. 1996, ApJL, 468, L85
Birkinshaw, M. 1999, Phys. Rep., 310, 97
Bond, J. R. et al., 2002, ApJ, submitted (astro-ph/0205386)
Bower, R. G. 1997, MNRAS, 288, 355
Carlstrom, J. E., Holder, G. P., & Reese, E. D. 2002, ARA&A, 40, 643
Cavaliere, A., Friedland, A., Gursky, H., & Spada, G. 1973, ApJ, 182, 405
Cavaliere, A. & Setti, G. 1976, A&A, 46, 81
Cayón, L. et al. 2000, MNRAS, 315, 757
Cole, S. & Kaiser, N. 1988, MNRAS, 233, 637
Condon, J. J. 1974, ApJ, 188, 279
Condon, J. J. & Dressel, L. L. 1978, ApJ, 222, 745
Condon, J. J. 1984, ApJ, 287, 461
Cooray, A. R., Grego, L., Holzapfel, W. L., Joy, M., & Carlstrom, J. E. 1998, AJ, 115, 1388
Cooray, A. 2000, Phys. Rev. D, 62, 103506
Cooray, A. 2001, Phys. Rev. D, 64, 63514
Cooray, A.& Melchiorri, A. 2002, Phys. Rev. D, accepted (astro-ph/0204250)
Dawson, K. S, Holzapfel, W. L., Carlstrom, J. E., LaRoque, S. J., Miller, A., Nagai, D. & Joy, M. 2002, ApJ, submitted (astro-ph/0206012)
de Luca, A., Desert, F. X., & Puget, J. L. 1995, A&A, 300, 335
Diego, J. M., Martínez-González, E., Sanz, J. L., Cayón, L., & Silk, J. 2001, MNRAS, 325, 1533
Eke, V. R., Cole, S., & Frenk, C. S. 1996, MNRAS, 282, 263
Ettori, S., De Grandi, S., & Molendi, S. 2002, A&A, 391, 841
Fabian, A. C. 1975, MNRAS, 172, 149
Ferreira, P. G., Magueijo, J., & Gorski, K. M. 1998, ApJ, 503, L1
Fischer, M. L. & Lange, A. E. 1993, ApJ, 419, 433
Franceschini, A., Toffolatti, L., Danese, L., & de Zotti, G. 1989, ApJ, 344, 35
Fomalont, E. B., Kellermann, K. I., Anderson, M. C., Weistrop, D., Wall, J. V., Windhorst, R. A., & Kristian, J. A. 1988, AJ, 96, 1187
Fomalont, E. B., Kellermann, K. I., Partridge, R. B., Windhorst, R. A., & Richards, E. A. 2002, AJ, 123, 2402
Fomalont, E. B., Partridge, R. B., Lowenthal, J. D., & Windhorst, R. A. 1993, ApJ, 404, 8

Haehnelt, M. G. & Tegmark, M. 1996, MNRAS, 279, 545
Hewish, A. 1961, MNRAS, 123, 167
Hobson, M. P. & Magueijo, J. 1996, MNRAS, 283, 1133
Holder, G. P. 2002, ApJL, submitted (astro-ph/0207633)
Holder, G. P. 2002b, ApJ, accepted (astro-ph/0205467)
Jenkins, A., Frenk, C. S., White, S. D. M., Colberg, J. M., Cole, S., Evrard, A. E., Couchman, H. M. P., & Yoshida, N. 2001, MNRAS, 321, 372
Kesden, M., Cooray, A. & Kamionkowski, M. 2002, Phys. Rev. D, submitted (astro-ph/0208325)
Kneissl, R., Jones, M. E., Saunders, R., Eke, V. R., Lasenby, A. N., Grainge, K., & Cotter, G. 2001, MNRAS, 328, 783
Komatsu, E. & Kitayama, T. 1999, ApJ, 526, L1
Komatsu, E. & Seljak,U. 2002, MNRAS, submitted (astro-ph/0205468)
Komatsu, E., Wandelt, B. D., Spergel, D. N., Banday, A. J., & Górski, K. M. 2002, ApJ, 566, 19
Korolev, V. A., Sunyaev, R. A., & Yakubsev, L. A. 1986, Soviet Astronomy Letters, 12, 339
Lin, H., Chiueh, T., & Wu, X. 2002, astro-ph/0202174
Longair, M. S., & Sunyaev, R. A. 1969, Nature, 223, 719
Luo, X. 1994, ApJ, 427, L71
Mason, B. S. et al., 2002, ApJ, submitted (astro-ph/0205384)
Mohr, J. J., Mathiesen, B., & Evrard, A. E. 1999, ApJ, 517, 627
Molnar, S. M. & Birkinshaw, M. 2000, ApJ, 537, 542
Ostriker, J. P. & Steinhardt, P. J. 1995, Nature, 377, 600
Padmanabhan, T. 1993, Structure formation in the universe. Cambridge, UK: Cambridge University Press
Peebles, P. J. E. 1993, Principles of physical cosmology. Princeton Series in Physics, Princeton, NJ: Princeton University Press.
Press, W. H. & Schechter, P. 1974, ApJ, 187, 425
Rowan-Robinson, M. & Fabian, A. 1974, MNRAS, 167, 419
Rubiño-Martín, J. A., Atrio-Barandela, F., & Hernández-Monteagudo, C. 2000, ApJ, 538, 53
Santos, M. G. et al. 2002, Physical Review Letters, 88, 241302
Sanz, J. L., Herranz, D., & Martínez-Gónzalez, E. 2001, ApJ, 552, 484
Sheth, R. K. & Tormen, G. 1999, MNRAS, 308, 119
Scheuer, P. A. G. 1957, Proc.Camb.Phil.Soc, 53, 764
Scheuer, P. A. G. 1974, MNRAS, 166, 329
Schulz, A. E. & White, M. 2002, ApJ submitted (astro-ph/0210667)
Seljak, U. ;, Burwell, J., & Pen, U. 2001, Phys.Rev.D, 63, 63001
Springel, V., White, M., & Hernquist, L. 2001, ApJ, 549, 681 [erratum: 2001, ApJ, 562, 1086]
Sunyaev, R. A. 1980, Soviet Astronomy Letters, 6, 213
Sunyaev, R. A. & Zeldovich, Y. B. 1970, Ap&SS, 7, 3
Sunyaev, R. A. & Zeldovich, Y. B. 1972, Comments on Astrophysics, 4, 173
Sunyaev, R. A. & Zeldovich, I. B. 1980, ARA&A, 18, 537
Taylor, A. C. et al. 2002, MNRAS, submitted (astro-ph/0205381)
Tegmark, M. & de Oliveira-Costa, A. 1998, ApJ, 500, L83
Toffolatti, L., Argueso Gomez, F., de Zotti, G., Mazzei, P., Franceschini, A., Danese, L., & Burigana, C. 1998, MNRAS, 297, 117
Viana, P. T. P. & Liddle, A. R. 1999, MNRAS, 303, 535
Zhang, P., Pen, U., & Wang, B. 2002, ApJ, 577, 555
Zeldovich, Y. B. & Sunyaev, R. A. 1969, Ap&SS, 4, 301

APPENDIX A: DEPENDENCE OF THE P(D) FUNCTION ON THE SCALING ASSUMPTIONS AND THE NORMALISATION σ_8

The scaling relation for the gas temperature used in this work was obtained from fittings to X-ray observations. However, we could also have used that one derived from the spherical collapse model, which takes the form (Eke, Cole, & Frenk 1996):

$$kT_{gas} = \frac{7.75}{\beta}\left(\frac{M}{10^{15}h^{-1}M_{\odot}}\right)^{2/3}(1+z)\left(\frac{\Omega_0}{\Omega(z)}\frac{\Delta_c}{178}\right)^{1/3} keV \quad (A1)$$

where Δ_c is the ratio of the mean density inside the virial radius to the critical density, and β is the ratio of the specific galaxy kinetic energy to specific gas thermal energy. This scaling has been used by other authors (e.g. Komatsu & Kitayama 1999; Molnar & Birkinshaw 2000). We will consider this scaling here to recompute the simulations, and we will show that the qualitative behaviour of the P(D) function and the skewness remains unchanged. We will adopt here $\beta = 1$, the same parameters describing the cluster ($r_{v0} = 1.3h^{-1}$ Mpc, $r_{c0} = 0.13h^{-1}$ Mpc, and $n_{c0} = 2 \times 10^{-3}$ cm^{-3}), and the same cosmological model as in the main text ($\Omega_m = 0.3$, $\Omega_\Lambda = 0.7$, $h = 0.67$, and $\sigma_8 = 0.9$). We integrate the PS mass function in the same range as in the main text.

Concerning the core evolution, in this work we have used an entropy-driven model with $\epsilon = 0$, which is described as:

$$r_c(M,z) = r_{c0}\left(\frac{M}{10^{15}h^{-1}M_{\odot}}\right)^{-1/6}\left(\frac{\Omega_0}{\Omega(z)}\frac{\Delta_c}{178}\right)^{-1/12}(1+z)^{(3\epsilon-1)/4} \quad (A2)$$

but without using the Δ_c factor. Therefore, we now repeat the computation taking it into account. A detailed study of how the power spectrum changes when assuming different core evolution models (a self-similar collapse, or an entropy-driven model with different values for the ϵ parameter), can be found in Komatsu & Kitayama (1999).

For definiteness, we will use the notation 'Model A' for the scaling relations used in the main text (derived from fittings to X-ray observations), and 'Model B' for the new scaling relations considered in this appendix. Figure A1 shows the resulting power spectrum (C_ℓ) and bispectrum (I_ℓ) for these two models. We can see that the qualitative behaviour of the bispectrum is the same.

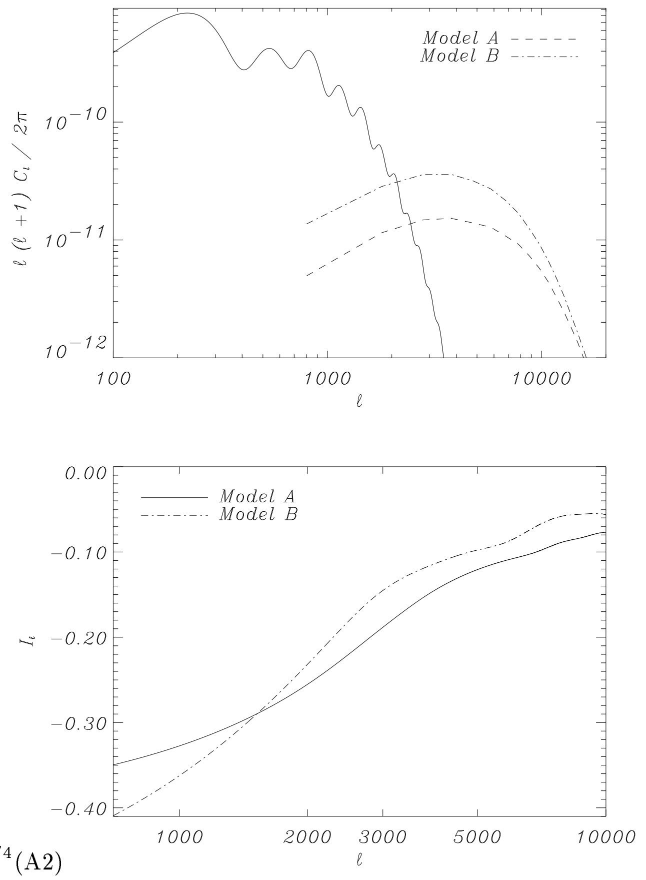

Figure A1. Top: Angular power spectrum for the SZ effect derived from Press-Schechter prescription, for two different models. These models (A and B) correspond to the same cosmological model, same normalisation ($\sigma_8 = 0.9$), but different scaling relations for the temperature and the core radius with the mass and redshift of the cluster (see details in text). The curves were obtained averaging 15 simulations (1°side) for each case. Bottom: Same as before, but for the bispectrum.

Figure A2 shows the P(D) function for these two models. Despite the different width of these curves (due to the different total power in the spectrum, see figure A1), when rescaling them by their σ ($\sigma^2 = \int D^2 P(D) dD$), the shape of both curves is very similar.

Finally, we have explored how the shape of the $P(D)$ is sensitive to the σ_8 value. We then obtain 15 simulations for each one of the following values of σ_8: 0.6, 0.7, 0.8, 0.9, 1.0 and 1.1, keeping the same cosmological model ($\Omega_m = 0.3$, $\Omega_\Lambda = 0.7$ and $h = 0.67$). For the scaling of the temperature and core radius with mass and redshift, we adopt the values of the 'Model B' described above.

It is well-known that the SZ angular power spectrum scales as $C_\ell \propto \sigma_8^{6--9}$ (see, e.g. Komatsu & Kitayama (1999)). In our particular case, our power spectra derived from the simulations shows an scaling $C_\ell \sim \sigma_8^9$. Figure A3 shows the obtained power spectra and bispectrum for these values. The shapes of the bispectrum curves change slightly when changing the value of σ_8. However, we can find an scaling for a given multipole. Given that SZ power spectrum peaks around $\ell \sim 3000$, we have done the study for $\ell = 3000$, obtaining that the bispectrum scales as $I_\ell \propto \sigma_8^{1.1}$.

The corresponding $P(D)$ functions are shown in figure A4, using a beam size of $\theta_b = 3'$. Given that we are particularly interested in the intermediate asymptotic region, we obtained the scaling of the 'a'–factor in that region ($P(D) \sim e^{aD}$). From our simulations, we have

$$a \approx 0.055\left(\frac{\sigma_8}{0.9}\right)^{4.5}\left(\frac{\theta_b}{2'}\right)^{-0.2} \qquad [\mu K^{-1}] \quad (A3)$$

for the region $1' \leqslant \theta_b \leqslant 5'$ and $0.6 \leqslant \sigma_8 \leqslant 1.1$. This is precisely the scaling with σ_8 that we would expect at first order, given that the shape of the $P(D)$ function is roughly proportional to the σ of the SZ map, and the latter is proportional to $C_\ell^{1/2}$. For illustration, in the lower panel of figure A4 we show the different $P(D)$ curves, rescaled by $D \rightarrow D\sigma_8^{-4.5}$,

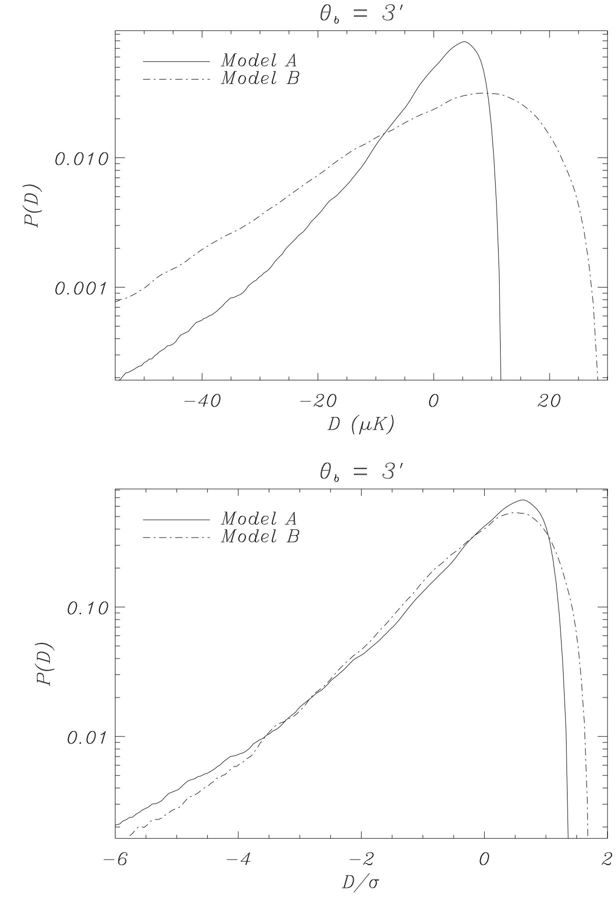

Figure A2. Top: P(D) functions for the two models considered in figure A1, smoothing the maps with a gaussian beam of size $\theta_b = 3'$. Bottom: Same figure, but rescaling the curves by their σ (obtained as $\sigma^2 = \int D^2 P(D) dD$.

for the case $\theta_b = 3'$. As we can see, their asymptotics become similar.

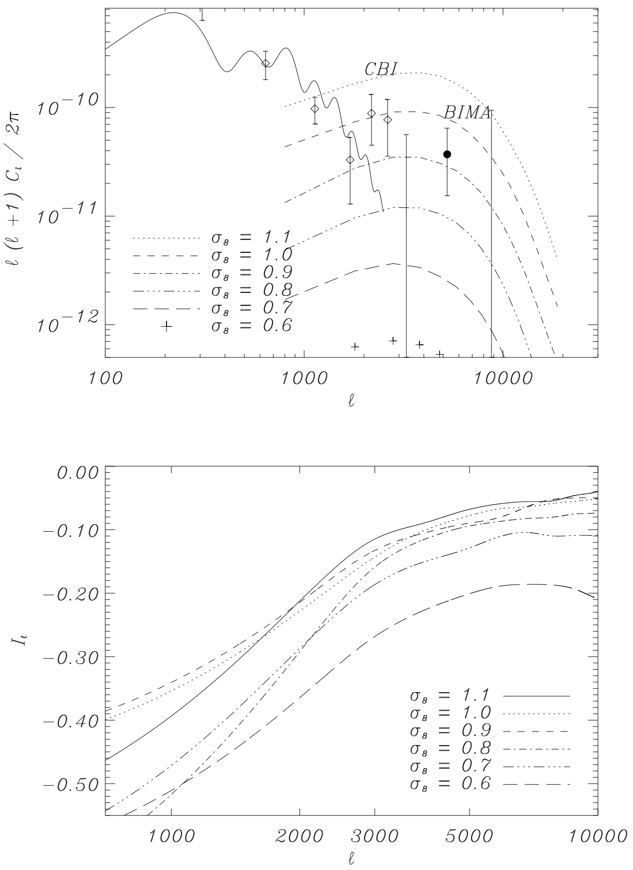

Figure A3. Top: Power spectrum of the SZ effect for different normalisations (σ_8 values). Each curve has been obtained from averaging 15 realizations of 1°size (error bars are not shown). For comparison, it is also shown the corresponding primordial CMB power spectrum, and the current observational measurements from CBI and BIMA. Bottom: Bispectrum of the SZ effect for the same values of σ_8 considered above.

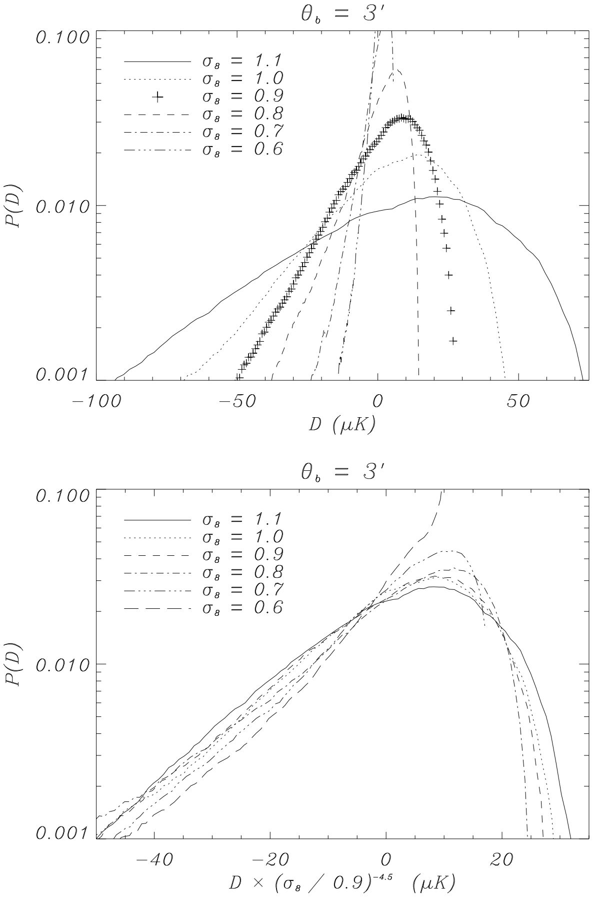

Figure A4. Top: P(D) curves for the same realizations considered in figure A3. The maps have been smoothed with a $3'$ FWHM gaussian beam. Bottom: Same P(D) curves, but rescaled by $D \rightarrow D\sigma_8^{-4.5}$. We can see that now the asymptotic regions are parallel.